

## Pyridine- $^{15}\text{N}$ — A Mobile NMR Sensor for Surface Acidity and Surface Defects of Mesoporous Silica

Ilja G. Shenderovich,<sup>†,‡</sup> Gerd Buntkowsky,<sup>†</sup> Andreas Schreiber,<sup>§</sup> Egbert Gedat,<sup>†</sup> Shasad Sharif,<sup>†</sup> Judith Albrecht,<sup>†</sup> Nikolaj S. Golubev,<sup>‡</sup> Gerhard H. Findenegg,<sup>§</sup> and Hans-Heinrich Limbach<sup>\*,†</sup>

*Institut für Chemie, Freie Universität Berlin, Takustrasse 3, D-14195 Berlin, Germany, Iwan-N.-Stranski-Institut für Physikalische und Theoretische Chemie, Technische Universität Berlin D-10623, Germany, and Institute of Physics, St. Petersburg State University, Ulianovskaja 1, 198904 St. Petersburg, Russia*

Received: April 11, 2003

The hydrogen bond interaction of pyridine with the silanol groups of the inner surfaces of MCM-41 and SBA-15 ordered mesoporous silica has been studied by a combination of solid-state NMR techniques. The pore diameters were varied between 3 and 4 nm for MCM-41 and between 7 and 9 nm for SBA-15.  $^1\text{H}$  MAS experiments performed under magic angle spinning (MAS) conditions in the absence and the presence of pyridine- $d_5$  reveal that the large majority of silanol groups are located in the inner surfaces, isolated from each other but able to form hydrogen bonds with pyridine. On the other hand, low- and room-temperature  $^{15}\text{N}$  CPMAS and MAS experiments (CP  $\equiv$  cross-polarization) performed on pyridine- $^{15}\text{N}$  show that at low concentrations all pyridine molecules are involved in hydrogen bonds with the surface silanol groups. In the presence of an excess of pyridine, a non-hydrogen-bonded pyridine phase is observed at 120 K in the slow hydrogen bond exchange regime and associates with an inner core phase. From these measurements, the number of pyridine molecules bound to the inner surfaces corresponding to the number of silanol groups could be determined to be  $n_{\text{OH}} \approx 3 \text{ nm}^{-2}$  for MCM-41 and  $\approx 3.7 \text{ nm}^{-2}$  for SBA-15. At room temperature and low concentrations, the pyridine molecules jump rapidly between the hydrogen-bonded sites. In the presence of an excess of pyridine, the hydrogen-bonded binding sites are depleted as compared to low temperatures, leading to smaller apparent numbers  $n_{\text{OH}}$ . Using a correlation established previously between the  $^{15}\text{N}$  and  $^1\text{H}$  chemical shifts and the NHO hydrogen bond geometries, as well as with the acidity of the proton donors, the distances in the pyridine–hydroxyl pairs were found to be about  $r_{\text{HN}} = 1.68 \text{ \AA}$ ,  $r_{\text{OH}} = 1.01 \text{ \AA}$ , and  $r_{\text{ON}} = 2.69 \text{ \AA}$ . This geometry corresponds in the organic solid state to acids exhibiting in water a  $\text{p}K_{\text{a}}$  of about 4. Room-temperature  $^{15}\text{N}$  experiments on static samples of pyridine- $^{15}\text{N}$  in MCM-41 at low coverage show a residual  $^{15}\text{N}$  chemical shift anisotropy, indicating that the jumps of pyridine between different different silanol hydrogen bond sites is accompanied by an anisotropic reorientational diffusion. A quantitative analysis reveals that in this regime the rotation of pyridine around the molecular  $C_2$  axis is suppressed even at room temperature, and that the angle between the Si–O axes and the OH axes of the isolated silanol groups is about  $47^\circ$ . These results are corroborated by  $^2\text{H}$  NMR experiments performed on pyridine- $4\text{-}d_1$ . In contrast, in the case of SBA-15 with the larger pore diameters, the hydrogen bond jumps of pyridine are associated with an isotropic rotational diffusion, indicating a high degree of roughness of the inner surfaces. This finding is correlated with the finding by  $^{29}\text{Si}$  CPMAS of a substantial amount of  $\text{Si}(\text{OH})_2$  groups in SBA-15, in contrast to the MCM-41 materials. The  $\text{Si}(\text{OH})_2$  groups are associated with surface defects, exhibiting not only silanol groups pointing into the pore center but also silanol groups pointing into other directions of space including the pore axes, leading to the isotropic surface diffusion. All results are used to develop molecular models for the inner surface structure of mesoporous silica which may be a basis for future simulations of the surfaces of mesoporous silica.

### Introduction

Since 10 years a new class of mesoporous silica materials has become available that constitute a two-dimensionally ordered array of cylindrical pores of uniform size disposed parallel to each other and separated by thin walls, as depicted schematically in Figure 1.<sup>1–23</sup> The pore diameter is adjustable between 2 and 4 nm in the case of MCM-41 silicas,<sup>1</sup> and between 6 and 12

nm for SBA-15 silica materials.<sup>3</sup> Silica formation takes place in aqueous media using surfactants or block copolymers as templating agents, and tetraethoxysilane (TEOS) as a silicate precursor. The silica materials are obtained as a fine powder after removal of the surfactant by calcination. Mesoporous silica materials are promising candidates for catalytic applications.<sup>3,4</sup> For these applications it is mandatory to understand the properties of the inner surfaces as well as the state of the guest molecules. Of particular importance is the chemical structure of the inner surfaces and walls, the type of the surface–guest as well as guest–guest interactions, and the mobility of the guest molecules. Such properties have been studied in the case of the

\* Corresponding author. Tel: (+49 30) 838 55375. Fax: (+49 30) 838 55310. E-mail: limbach@chemie.fu-berlin.de.

<sup>†</sup> Freie Universität Berlin.

<sup>‡</sup> St. Petersburg State University.

<sup>§</sup> Technische Universität Berlin.

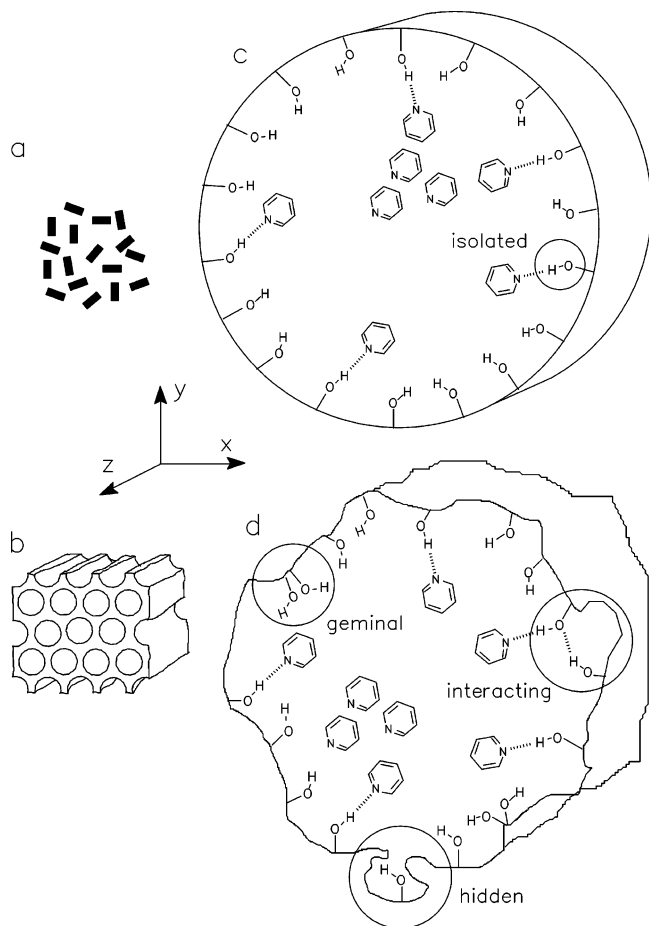


**Figure 1.** Polycrystalline mesoporous silica powders (schematically) as host for pyridine- $^{15}\text{N}$ . The latter can form hydrogen bonds with all surface OH groups or with additional water or form a bulk core phase. (a) Isotropic distribution of polycrystallites in an external magnetic field  $B_0$ . (b) Cylindrical pores of a given crystallite. The  $z$  axis corresponds to the cylinder axis. (c) Cylindrical inner surface pore model with regular arranged isolated surface Si-OH groups. The molecular reorientation of pyridine is anisotropic. (d) Pore model exhibiting a "rough" inner surface, containing "isolated" and "interacting" SiOH groups as well as "geminal"  $\text{Si}(\text{OH})_2$  groups. The molecular reorientation of pyridine is isotropic.

related zeolites by various INS and NMR techniques.<sup>5–9</sup> Much less is known about the noncrystalline host–guest behavior of mesoporous silica materials where a molecular model of the inner silica surface is still lacking.

The complexity of the materials arises from (i) the flexibility of the Si–O–Si bond angle, (ii) the occurrence of different classes of silicon atoms in the inner surfaces labeled as  $Q^{4-n}$ , which are distinguished by the number  $n$  of OH groups attached to Si, and (iii) a variation of the hydrogen bond properties and the acidity of the OH groups. The properties of the latter depend on the type and method of preparation of the material studied.<sup>10–13</sup> Methods to determine the number of OH groups  $n_{\text{OH}}$  in the inner surfaces of silica materials have been reviewed recently.<sup>14</sup> For mesoporous silica materials  $n_{\text{OH}}$  has been estimated by thermogravimetry<sup>15</sup> and by silylation<sup>16</sup> of the OH groups to be about  $2\text{--}2.5\text{ nm}^{-2}$ . By quantitative  $^{29}\text{Si}$  CPMAS NMR values of about  $2.5$  to  $4\text{ nm}^{-2}$  were estimated.<sup>17</sup> Much smaller values around  $1\text{ nm}^{-2}$  are obtained by IR spectroscopy of adsorbed pyridine.<sup>18</sup> The surface areas were determined in these cases by the BET method.<sup>19</sup> Values of  $4.9\text{ nm}^2$  have been determined by exchange with  $\text{D}_2\text{O}$  suggested for normal silica surfaces, where the values do not depend in a significant way on the type of silica but

strongly on the sample treatment after the synthesis.<sup>20</sup> For example, after a vacuum treatment at  $1373\text{ K}$  the number of surface OH groups can be reduced to less than  $0.15$  per  $\text{nm}^2$ .  $\text{Si}(\text{OH})_3$  groups ( $Q^1$  silicon) are rare, as calcination leads to an interconversion of  $Q^2$  and  $Q^3$  into  $Q^4$ .<sup>21</sup>

The silica lattice mainly consists of  $Q^4$  silicon. As the chemical shielding of the  $^{29}\text{Si}$  nuclei depends on the number of attached OH groups the distribution of  $Q^1$  to  $Q^4$  silicon can be estimated by  $^{29}\text{Si}$  NMR spectroscopy under the conditions of magic angle spinning (MAS) and cross-polarization.<sup>11</sup> By contrast, the different hydrogen bond types cannot be determined using this method. Therefore, to our knowledge, a more detailed analysis of the surface structure is still lacking.

In Figure 1c,d different classes of SiOH groups are illustrated. The abundant OH groups are attached to  $Q^3$  silicon atoms, but geminal OH groups attached to  $Q^2$  silicon atoms may also occur. The OH groups may exhibit different hydrogen bond properties. According to the notation of Ugliengo et al.<sup>22</sup> "isolated" OH groups are not involved in a hydrogen bond with another OH group, whereas "interacting" OH groups are involved in such bonds. Geminal OH groups attached to  $Q^2$  silicon cannot form with each other hydrogen bonds. One can furthermore distinguish OH groups which are located in the surfaces in such a way that they are able to form hydrogen bonds to added proton acceptors, and those who are unable to form such bonds. We will call the former "surface" OH groups and the latter "hidden" OH groups. Because of space requirements of an added proton donor as a guest molecule, not all surface OH groups may form host–guest hydrogen bonds at the same time.

Furthermore, in the scenario of Figure 1c the case of an ideal cylindrical pore with regularly arranged isolated SiOH groups is illustrated. The groups are "isolated", exhibiting an average distance of  $5\text{--}7\text{ \AA}$  between neighboring groups, in agreement with a finding of about  $2\text{--}4$  OH groups per  $\text{nm}^2$ . These distances exclude the occurrence of interacting SiOH groups involved in mutual hydrogen bonding. The Si–O axes of the SiOH groups all point more or less into the pore center. On the other hand, one can conceive a "rough" pore surface (Figure 1d) with irregularly arranged surface SiOH groups of all types, where the Si–O axes of the SiOH groups point in all directions of space. Such an irregular surface may contain interacting SiOH groups that are close in space although attached to silicon atoms that are further away from each other.

In the past years, some of us have characterized the interactions of molecular guests with silica hosts by solid-state NMR spectroscopy. It was shown by  $^2\text{H}$  NMR spectroscopy that the rotational characteristics of benzene in mesoporous silica are very different from bulk benzene.<sup>23</sup> On the other hand, heterocyclic molecules such as pyrazole that contain both proton donor and acceptor groups, when incorporated in amorphous alumina and silica,<sup>24</sup> are subject to hydrogen bonding and complicated proton exchange reactions with Si–OH groups, and to surface diffusion. A simpler proton acceptor is pyridine, for which it has been shown using solid state  $^{15}\text{N}$  CPMAS NMR that the isotropic  $^{15}\text{N}$  chemical shift is modulated when the molecule is incorporated into different sites of acid zeolites<sup>25</sup> or amorphous alumina.<sup>26</sup> In particular, a substantial high field shift occurs when pyridine is protonated. The influence of hydrogen bonding and protonation of pyridine on NMR parameters has been studied by some of us in more detail using low-temperature NMR methods. It has been shown that for 1:1 hydrogen-bonded complexes of an acid (AH) with pyridine (B) an increase of the acidity of AH leads to a gradual proton dislocation from a molecular complex to a zwitterionic complex

$A-H\cdots B \leftrightarrow A^{\delta-}\cdots H\cdots B^{\delta+} \leftrightarrow A^-\cdots H-B^+$ .<sup>27</sup> This dislocation can also be induced by an increase of the polarity of the solvent when the temperature is lowered.<sup>28</sup> By crystallizing a number of 1:1 complexes of 2,4,6-trimethylpyridine (collidine)-<sup>15</sup>N with a number of different acids a correlation of the <sup>15</sup>N NMR isotropic and anisotropic chemical shifts with the dipolar <sup>2</sup>H–<sup>15</sup>N couplings and hence the nitrogen–hydrogen distances and  $pK_a$  values has been observed using solid state NMR.<sup>29</sup> These correlations allow us now to explore the nitrogen–hydrogen distance distribution function of pyridine and its derivatives in mesoporous solids, as some of us have shown in a preliminary communication, that it is possible to obtain solid state <sup>15</sup>N NMR spectra of pyridine-<sup>15</sup>N in mesoporous solids.<sup>30</sup> On the other hand, the diffusion coefficient of pyridine in these materials was found to be strongly reduced as compared to bulk pyridine, which was attributed to hydrogen bonding to hydroxyl groups of the inner surfaces.<sup>31</sup>

The first scope of this study was, therefore, to detect and characterize the proton donating power and the geometry of the surface Si–OH $\cdots$ pyridine hydrogen bonds in mesoporous silica of the MCM-41 and SBA-15 types exhibiting different pore diameters, using <sup>15</sup>N and <sup>29</sup>Si NMR. The second scope was to derive from the experiments a more detailed model of the inner silica surfaces, because we expected an anisotropic reorientation of pyridine in a regular cylindrical pore (Figure 1c) and a quasi-isotropic reorientation in a nonregular surface (Figure 1d).

After the Experimental Section, in which details of the sample preparation and experiments are described, we report the results of our NMR experiments. Because of the high mobility of the guest molecules at room temperature,<sup>24</sup> it was necessary to perform low-temperature <sup>15</sup>N CPMAS NMR experiments on <sup>15</sup>N labeled pyridine in a regime where hydrogen bond exchange is slow. By performing additional room-temperature experiments with and without MAS the anisotropy of the reorientation of pyridine in the pores was studied. Further information about the surfaces was obtained by <sup>29</sup>Si CPMAS, <sup>1</sup>H MAS NMR of fully deuterated pyridine, and by <sup>2</sup>H MAS NMR experiments on pyridine singly deuterated in the para-position. In the subsequent discussion, the main elements of our findings are used to set up cartoons of the inner surface of mesoporous silica, the SiOH proton donor strength and acidity, and of the motions of pyridine in these materials from which information about the roughness and surface defects is obtained. In particular, it is shown that a large variety of mesoporous silica surfaces can be generated by combining six-membered tridymite SiO<sub>2</sub> units in different ways. These surfaces can reproduce the experimental findings.

## Experimental Section

**Materials.** The SBA-15 samples were prepared according to the synthesis of Zhao et al.<sup>3</sup> employing a technical-grade PEO–PPO–PEO triblock copolymer (Pluronic P123, BASF Corp., Mount Olive, NJ) as the templating agent. A 4 wt % aqueous solution of P123 was treated with aqueous HCl or H<sub>2</sub>SO<sub>4</sub> to reach a pH of ca. 1.5. Tetraethoxysilane (TEOS) was added to this solution under stirring at 35 °C. The precipitated product was kept in the reaction solution at 35 °C for 24 h and then at 95 °C for another 12–24 h, to generate materials of different pore diameters. After rinsing with pure water and drying at 105 °C, the powder was heated to 180 °C in air for 4 h to remove most of the polymer and finally calcinated at 550 °C under flowing air.

The MCM-41 samples were synthesized following the procedure of Grün et al.<sup>32</sup> in aqueous ammonia solutions, using

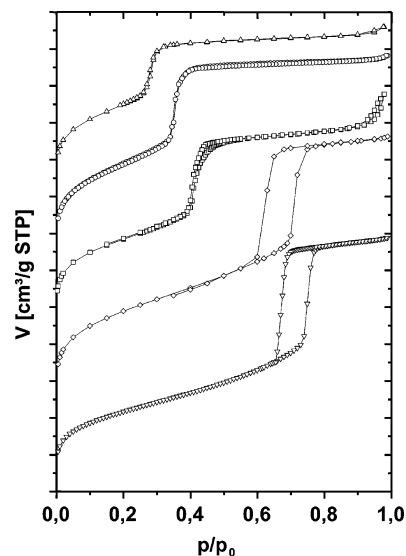


**Figure 2.** Nitrogen adsorption isotherms (77 K) in the MCM-41 (a–c) and SBA-15 (d, e) materials.

C<sub>14</sub>–, C<sub>16</sub>–, and C<sub>18</sub>–trimethylammonium bromide as template molecules and again TEOS as the silicate precursor. The precipitated products were heat-treated, dried, and calcinated in a manner similar to that for SBA-15. Details of the synthesis are given elsewhere.<sup>33</sup>

**Synthesis of Pyridine-4-*d*<sub>1</sub> C<sub>5</sub>H<sub>4</sub>DN.** The synthesis of this molecule was in analogy to the procedure described by Hildebrandt et al.<sup>34</sup> for the replacement of p-halogen in substituted pyridine molecules by deuterium. A total of 11.0 g (73.8 mmol) of 4-chloropyridine hydrochloride was dissolved in 200 mL of D<sub>2</sub>O. The solution was neutralized with 6.19 g (73.8 mmol) of NaHCO<sub>3</sub>, and 11.7 mL (215 mmol) of 96% D<sub>2</sub>SO<sub>4</sub> was added dropwise under stirring. A 13.6 g (208 mmol) amount of Zn was added in small quantities under strong evolution of gas. The solution was heated under reflux for 4 h and then cooled to room temperature. It was neutralized with 85 g of NaHCO<sub>3</sub> and the precipitated Zn(OH)<sub>2</sub> filtered and washed with distilled water. To obtain the product, the filtrate was extracted four times with 200 mL of CH<sub>2</sub>Cl<sub>2</sub>. The latter was then removed under normal pressure. A total of 2 g of raw p-*d*-pyridine was obtained, which was purified by distillation in a bulb tube at 150 °C and 800 mbar. The final product was characterized by mass and <sup>1</sup>H liquid-state NMR spectroscopy. Yield: 2 g (34.0%) of C<sub>5</sub>H<sub>4</sub>DN, with a deuterium fraction of 85.9% as determined by mass spectroscopy.

**Characterization.** Nitrogen adsorption isotherms at 77 K were measured by gas volumetry using a Gemini-2375 apparatus (Micromeritics). For all materials the isotherms (Figure 2) exhibit a rather sharp step due to pore condensation, indicating a narrow pore size distributions. Powder X-ray diffraction (XRD) measurements were made on a Kratky camera using the Cu K $\alpha$  radiation with Ni foil as a filter. The diffraction patterns exhibit five peaks (MCM-41) or three peaks (SBA-15), which can be assigned to a 2D-hexagonal lattice. Details of the characterization are given in ref 32. The BET specific surface area, the specific pore volume, and the pore width (determined by the method of Dollimore and Heal) as derived from the nitrogen adsorption isotherm in the different samples are summarized in Table 1.

**Sample Preparation.** The composition of the silica–pyridine samples measured in this study is described in Table 1. To obtain reproducible results, most samples were prepared using vacuum techniques as follows. Mesoporous silica was loaded into a



TABLE 1: Mesoporous Silica Samples Studied in This Work

| sample    | silica type            | $a_0$ /nm | $d$ /nm | $A$ /m <sup>2</sup> g <sup>-1</sup> | $V_p$ /cm <sup>3</sup> g <sup>-1</sup> | silica/mg | pyridine type                                 | pyridine/mg | NMR                              | glass insert |
|-----------|------------------------|-----------|---------|-------------------------------------|--|-----------|---|-------------|----------------------------------|--------------|
| <b>a</b>  | MCM- 41                | 4.0       | 2.9     | 1180                                | 0.79                                   | 10        | C <sub>5</sub> H <sub>5</sub> <sup>15</sup> N | 2           | <sup>15</sup> N                  | yes          |
| <b>b1</b> | MCM- 41                | 4.6       | 3.3     | 1010                                | 0.89                                   | 10        |   |             | <sup>29</sup> Si                 | no           |
| <b>b2</b> | MCM- 41                | 4.6       | 3.3     | 1010                                | 0.89                                   | 10        | C <sub>5</sub> H <sub>5</sub> <sup>15</sup> N | 2           | <sup>15</sup> N                  | yes          |
| <b>c1</b> | MCM- 41                | 4.9       | 3.7     | 870                                 | 0.99                                   | 10        |   |             | <sup>29</sup> Si, <sup>1</sup> H | no           |
| <b>c2</b> | MCM- 41                | 4.9       | 3.7     | 870                                 | 0.99                                   | 10        | C <sub>5</sub> H <sub>5</sub> <sup>15</sup> N | 2           | <sup>15</sup> N                  | yes          |
| <b>c3</b> | MCM- 41                | 4.9       | 3.7     | 870                                 | 0.99                                   | 10        | C <sub>5</sub> H <sub>5</sub> <sup>15</sup> N | 5           | <sup>15</sup> N                  | yes          |
| <b>c4</b> | MCM- 41                | 4.9       | 3.7     | 870                                 | 0.99                                   | 5         | C <sub>5</sub> D <sub>5</sub> N               | 5           | <sup>1</sup> H                   | no           |
| <b>c5</b> | MCM- 41                | 4.9       | 3.7     | 870                                 | 0.99                                   | 10        | C <sub>5</sub> H <sub>4</sub> (p-D)N          | 2           | <sup>2</sup> H                   | yes          |
| <b>d</b>  | SBA-15                 | 10.4      | 7.5     | 870                                 | 1.05                                   | 10        | C <sub>5</sub> H <sub>5</sub> <sup>15</sup> N | 2           | <sup>15</sup> N                  | yes          |
| <b>e1</b> | SBA-15                 | 11.1      | 8.9     | 750                                 | 1.06                                   | 10        |   |             | <sup>29</sup> Si, <sup>1</sup> H | no           |
| <b>e2</b> | SBA-15                 | 11.1      | 8.9     | 750                                 | 1.06                                   | 10        | C <sub>5</sub> H <sub>5</sub> <sup>15</sup> N | 2           | <sup>15</sup> N                  | yes          |
| <b>e3</b> | SBA-15                 | 11.1      | 8.9     | 750                                 | 1.06                                   | 10        | C <sub>5</sub> H <sub>5</sub> <sup>15</sup> N | 5           | <sup>15</sup> N                  | yes          |
| <b>e4</b> | SBA-15                 | 11.1      | 8.9     | 750                                 | 1.06                                   | 5         | C <sub>5</sub> D <sub>5</sub> N               | 5           | <sup>1</sup> H                   | no           |
| <b>e5</b> | SBA-15 water saturated | 11.1      | 8.9     | 750                                 | 1.06                                   | 10        | C <sub>5</sub> H <sub>5</sub> <sup>15</sup> N | 5           | <sup>15</sup> N                  | yes          |

<sup>a</sup>  $a_0$ , pore to pore distance from XRD measurements;  $d$ , pore width from the adsorption branch of the nitrogen isotherm;  $A$ , BET specific surface area;  $V_p$ , specific pore volume.

glass-insert (Wilmad, Buena, NY) for Chemagnetics 6 mm rotors and attached to a vacuum line. To remove physisorbed and hydrogen-bonded water without causing dehydroxylation of silanol groups,<sup>15</sup> the silica was dried under high vacuum at approximately 10<sup>-6</sup> mbar for 24 h at a moderate temperature of 150 °C. Then, small amounts of water-free pyridine were condensed into the sample. Pyridine (98% <sup>15</sup>N enriched) was purchased from Chemotrade, Leipzig. The inserts were detached from the vacuum line by flame sealing approximately 10 cm above the sample. The sealed samples were then mounted in a lathe, home-built according to the design of Hunger,<sup>35</sup> and flame sealed while the sample was spun, to achieve the cylinder symmetry necessary for the high-speed MAS. In the case of sample **e5**, the silica material was stored for 24 h at approximately 30% relative humidity produced by a saturated aqueous solution of MgCl<sub>2</sub> before the sample preparation. The samples used in the <sup>1</sup>H MAS NMR experiments were prepared as follows. Approximately 5 mg of silica were loaded into a 4 mm NMR rotor and the sample dried under high vacuum (ca. 10<sup>-6</sup> mbar) for 24 h at a moderate temperature of 150 °C. A first <sup>1</sup>H MAS NMR spectrum was then measured immediately after closing the rotor. Afterward the rotor was opened and 5 mg of 99% ring-deuterated pyridine-*d*<sub>5</sub> (Deutero) was added to the sample. The rotor was again closed and the second NMR spectrum was measured. As a result, some traces of water may be adsorbed on the silica surface during the sample preparation.

**NMR Measurements.** All <sup>15</sup>N and <sup>29</sup>Si NMR measurements were performed on a Bruker MSL-300 instrument, operating at 7 T, equipped with a Chemagnetics-Varian variable-temperature 6 mm pencil CPMAS probe. The <sup>29</sup>Si spectra were recorded employing the {<sup>1</sup>H}-<sup>29</sup>Si CPMAS NMR experiment. Following the procedure described in ref 36, a relatively long cross-polarization (CP) contact time of 15 ms was employed. This long CP time ensures sufficient polarization transfer to all different species of silica, i.e., Q<sup>2</sup>, Q<sup>3</sup>, and Q<sup>4</sup>. The <sup>29</sup>Si chemical shifts are referenced to liquid TMS. The room-temperature <sup>15</sup>N static and magic angle spinning (MAS, 6000 Hz) NMR experiments were performed employing a  $\pi/2$  pulse-sequences and proton decoupling. The low-temperature <sup>15</sup>N MAS measurements at 120 K were performed employing the {<sup>1</sup>H}-<sup>15</sup>N CPMAS technique with a cross-polarization contact time of 5 ms. All <sup>15</sup>N chemical shift values are referenced to solid <sup>15</sup>NH<sub>4</sub>Cl. A typical 90° pulse length was 8  $\mu$ s for <sup>1</sup>H and <sup>15</sup>N and 4  $\mu$ s for <sup>29</sup>Si.

The <sup>2</sup>H NMR experiments were performed on a home-built three channel NMR spectrometer<sup>37,38</sup> at a field of 6.98 T, corresponding to a <sup>2</sup>H resonance frequency of 45.7 MHz on a standard Oxford wide bore magnet (89 mm) equipped with a room-temperature shim unit. For the <sup>2</sup>H-channel a 2 kW class

AB amplifier from AMT equipped with an RF-blanking for suppressing the noise during data acquisition was employed. The RF was fed through a crossed diode duplexer, connected to the detection preamplifier and through the filters into the probe. The <sup>2</sup>H pulse width was 3.0  $\mu$ s, corresponding to 83 kHz B<sub>1</sub>-field in frequency units.

All <sup>2</sup>H NMR experiments were performed using a home-built 5 mm <sup>2</sup>H NMR probe. The probe was placed in a dynamic Oxford CF1200 helium flow cryostat. The sample temperature was controlled employing an Oxford ITC 503 temperature controller. During cooling and before and after data acquisition the sample temperature was directly controlled via a Cernox sensor placed in the direct vicinity of the sample. This temperature was used to calibrate the readings of a second CGR-1-1000 sensor, which is part of the cryostat. During data acquisition, the first sensor was disconnected from the ITC 503 and grounded to protect the ITC from the RF and to avoid distortions of the signal. The <sup>2</sup>H NMR spectra were recorded using the solid echo technique, with an echo spacing of 30  $\mu$ s and a full 32-step phase cycle. Before Fourier transformation the echo-signal was phase corrected and the imaginary part zeroed to give fully symmetric spectra. The repetition time of the measurements was 3 s at 292 K and 1 s at 175 K. The number of accumulations was 73 504 scans at 292 K and 98 944 scans at 175 K.

<sup>1</sup>H MAS NMR experiments were carried out at 300.13 MHz on a Bruker MSL-300 instrument equipped with a Bruker 4 mm probe. Single pulse excitation has been applied, the repetition time of the measurements was 15 s and the MAS rate was about 10 kHz.

The static <sup>15</sup>N and <sup>2</sup>H NMR spectra were simulated employing a laboratory written Matlab program. Instead of numerically performing the powder integration, the faster analytical expression of the powder pattern in terms of elliptic integrals<sup>39</sup> was used to calculate the line shape for zero width. The resulting Pake spectra were numerically convoluted with a Lorentzian by Fourier transformation into the time domain, multiplied with a decaying exponential function and transformed back into the frequency domain.

## Results

We report in this section the results of our solid-state NMR measurements. The samples were characterized by the following experiments: (i) <sup>29</sup>Si CPMAS NMR to obtain information on the type of silicon atoms, (ii) <sup>1</sup>H MAS NMR measurements at room temperature with and without pyridine-*d*<sub>5</sub> to obtain information about the type and location of the silanol groups, (iii) <sup>15</sup>N CPMAS NMR measurements of pyridine-<sup>15</sup>N at low

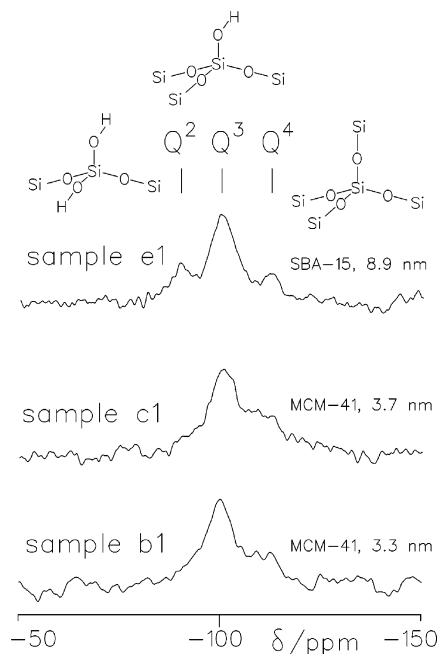


**Figure 3.** Solid-state  $\{^1\text{H}\}$ - $^{29}\text{Si}$  CPMAS spectra at 300 K of the silica samples **b1**, **c1** (MCM-41), and **e1** (SBA-15), respectively.

temperature to obtain information about the details of hydrogen bonding between pyridine and the silanol groups, (iv) room-temperature  $^{15}\text{N}$  NMR experiments of pyridine- $^{15}\text{N}$  to obtain information about the anisotropy of the motion of pyridine, and (v)  $^2\text{H}$  NMR measurements of pyridine- $4-d_1$  to check the type of the motion of pyridine motion in an independent way.

#### $^{29}\text{Si}$ CPMAS NMR Measurements at Room Temperature.

The main purpose of these experiments was the characterization of the samples with respect to the different possible species of silicon. From the literature<sup>17,36,40,41</sup> it was known that the  $\text{Q}^2$ ,  $\text{Q}^3$ , and  $\text{Q}^4$  species resonate at about  $-90$ ,  $-100$ , and  $-110$  ppm, respectively. In particular we were interested to see whether there are differences in the distribution of the hydroxyl groups on the surface of MCM-41 and SBA-15 silica.

In Figure 3 are depicted the room-temperature  $^{29}\text{Si}$  NMR CPMAS spectra of the silica samples **b1**, **c1** (MCM-41), and **e1** (SBA-15). In all three samples the dominating signal corresponds to the  $\text{Si}(\text{OH})$  or  $\text{Q}^3$  silicon nuclei.  $\text{Q}^4$  leads to a small peak at higher field. In the SBA-15 sample a low-field peak arising from  $\text{Si}(\text{OH})_2$  groups  $\text{Q}^2$  is clearly resolved, but not in the MCM-41 samples. As the CP technique was used, relative signal intensities within each spectrum depend in a complicated way on the dipolar  $^{29}\text{Si}$ - $^1\text{H}$  couplings and hence the corresponding distances. However, from the comparison of the three spectra in Figure 3 we can conclude that there are much fewer  $\text{Si}(\text{OH})_2$  groups  $\text{Q}^2$  in the MCM-41 samples as compared to the SBA-15 sample. This finding is significant and will constitute later an important element for modeling the silica surfaces in both materials.

#### $^1\text{H}$ MAS NMR Measurements at Room Temperature.

In Figure 4 are depicted some typical room-temperature  $^1\text{H}$  NMR MAS spectra of the silica samples **c1** (MCM-41) and **e1** (SBA-15) where water had been removed under high vacuum (ca.  $10^{-6}$  mbar) for 24 h at  $150^\circ\text{C}$ . Both samples exhibit a proton resonance at  $1.77 \pm 0.05$  ppm, in agreement with the literature.<sup>16</sup> This peak has been attributed to isolated silanol hydroxyl groups of mesoporous silica.

For comparison, we depict in Figure 4 the  $^1\text{H}$  NMR MAS spectra of samples **c4** and **e4** that were obtained from samples

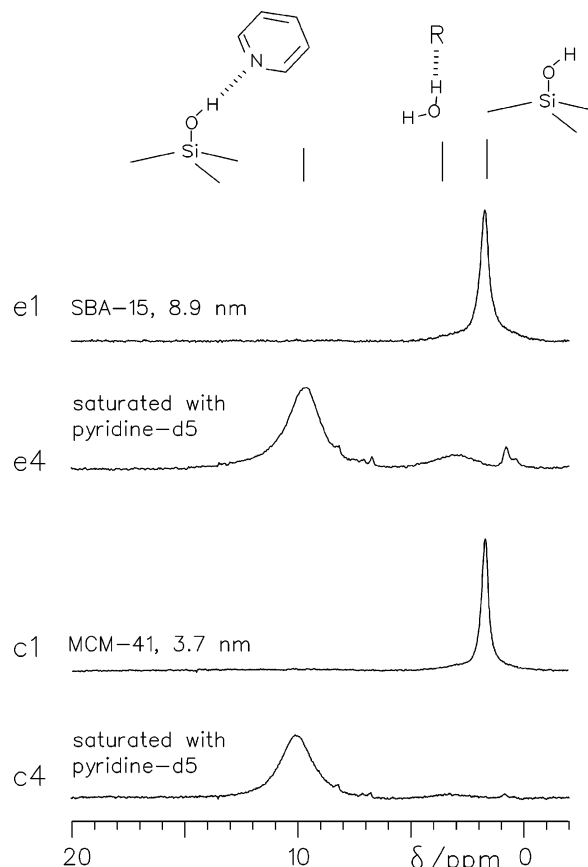


**Figure 4.** Room-temperature  $^1\text{H}$  MAS spectra of the silica samples **c1** (MCM-41) and **e1** (SBA-15) (upper) and the same samples with an excess of ring-deuterated pyridine- $d_5$ , **c4** and **e4** (lower), respectively.

**c1** and **e1** by adding deuterated pyridine to such an extent that the inner pores are filled. The dominant effect is that the silanol signal is now shifted to about  $9.9 \pm 0.2$  ppm. This effect indicates that the silanol groups are now hydrogen bonded to pyridine. As only silanol groups in the inner surfaces are accessible to hydrogen bonding with pyridine, this result indicates that most silanol groups arise from the inner surfaces but not from walls or small pores, which are not accessible to pyridine. We did not check the origin of the increased line width of the low-field signal, which could arise either from the sample inhomogeneity or from proton exchange with traces of water.

In addition to the low-field signal, a weak and broad signal appears in the SBA-15 sample around 3 ppm; the corresponding signal is smaller in the case of the MCM-41 sample. A careful look at the spectra indicates that this signal is also present already before the addition of pyridine, where it is difficult to detect because of the large intensive signal of the isolated  $\text{SiOH}$  groups. Therefore, we assign this signal to weakly interacting hidden silanol groups. A weak sharp signal at  $0.85 \pm 0.05$  ppm could not be assigned. It is likely that it stems from organic residues remaining from the synthesis.

#### $^{15}\text{N}$ CPMAS NMR Measurements at Low Temperature.

To explore hydrogen-bonded sites of pyridine- $^{15}\text{N}$  in mesoporous silica by  $^{15}\text{N}$  NMR, it is necessary to suppress hydrogen bond exchange of this molecule between different sites. This was achieved by performing low-temperature  $^{15}\text{N}$  CPMAS NMR experiments around 120 K on various samples. Some typical results are depicted in Figure 5. The spectra of samples **a**, **b2**, **c2**, **d**, and **e2**, where the amount of pyridine adsorbed on the surface is too small to cover the whole inner surface, exhibit a single broad pyridine- $^{15}\text{N}$  signal at  $251.5 \pm 0.5$  ppm. For com-

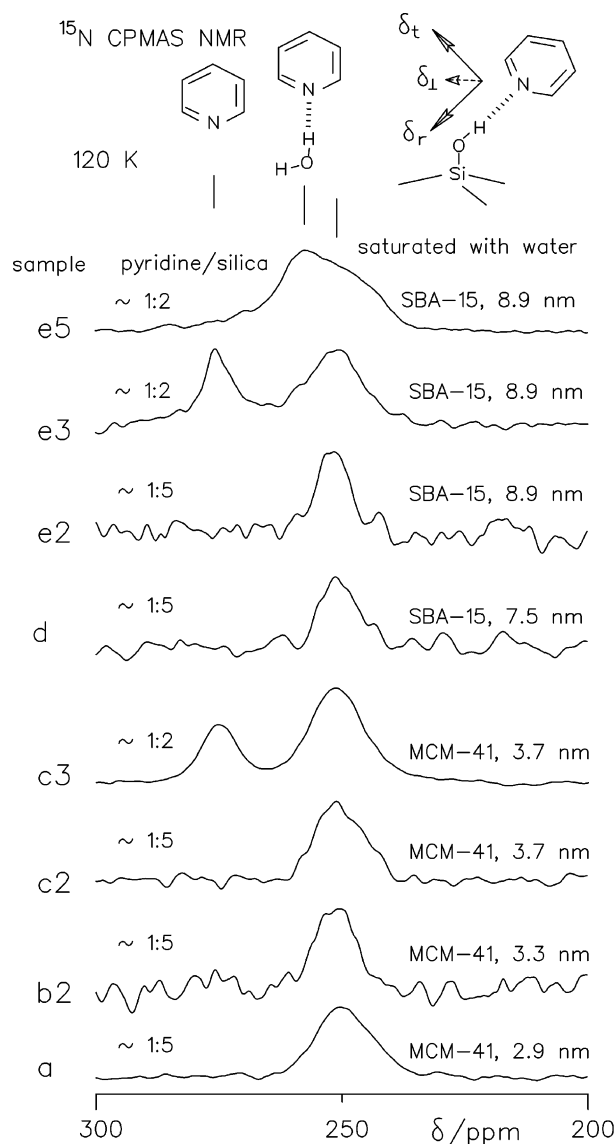


**Figure 5.** Solid-state  $\{^1\text{H}\}$ - $^{15}\text{N}$  CPMAS spectra at 120 K of pyridine loaded onto the silica samples **a**, **b2**, and **c2** (MCM-41) and **d** and **e2** (SBA-15), respectively; onto the same silica with an excess of pyridine (**c3**, **e3**), and onto a SBA-15 sample containing water (**e5**). Silica/pyridine weight per weight loading: samples **a**–**e2**, 10 mg/2 mg, and samples **c3**, **e3**, **e5**, 10 mg/5 mg.

parison, in the spectra of samples **c3** and **e3** an additional line at 276 ppm is visible. This position is typical for non-hydrogen-bonded pyridine- $^{15}\text{N}$ .<sup>29</sup> Thus, we assign the signal at 251.5 ppm to pyridine hydrogen bonded to silanol groups of the inner silica surface. The chemical shifts and hence, as will be discussed later in detail, the hydrogen bond geometries are almost independent of the silica material type and independent of the pyridine mole fraction. The spectra show in all cases no traces of pyridinium cations, which are expected below 170 ppm.<sup>29</sup>

To confirm that pyridine is hydrogen bonded to SiOH groups and not to residual water, we measured also the spectra of sample **e5** (Figure 5 top), which had been exposed to a humid gas atmosphere. We observe a broad signal consisting of two components around 259 and around 250–240 ppm. Some preliminary experiments at 120 K on solid frozen pyridine- $^{15}\text{N}$ /water mixtures indicate that the 259 ppm signal corresponds to pyridine hydrogen bonded to some water molecules. The signal between 250 and 240 ppm may both correspond to  $\text{SiOH}\cdots\text{pyridine}$  and/or  $\text{SiOH}\cdots\text{water}\cdots\text{pyridine}$  species. Any-

way, these results indicate that the standard procedure used in this work to prepare the other samples was sufficient to remove physisorbed water.

In conclusion, the signal at 251 ppm corresponds to pyridine involved in hydrogen bonds with the surface hydroxyl groups. We associate the broadness of the lines not to a homogeneous but to an inhomogeneous broadening arising from a distribution of chemical shifts corresponding to small variations in the  $\text{H}\cdots\text{N}$  bond distances as will be discussed below.

**$^{15}\text{N}$  MAS and Static NMR Measurements at Room Temperature.** To obtain further information about the pyridine mobility in mesoporous silica, we have measured additionally the room-temperature  $^{15}\text{N}$  NMR spectra of the samples of Figure 5, both under static and MAS conditions, using a  $\pi/2$  pulse-sequence. This sequence was employed because of the liquid type mobility of pyridine at room temperature. The results are depicted in Figure 6. Let us first describe the  $^{15}\text{N}$  MAS spectra of samples **a**, **b2**, **c2**, **d**, and **e2** containing pyridine in low concentrations. Here, single sharp lines are observed, exhibiting the same chemical shifts as the corresponding low-temperature signals; however, the lines are now much sharper. By contrast, the  $^{15}\text{N}$  NMR spectra of the static samples exhibit interesting differences. The signals of the SBA-15 samples **d** and **e2** are relatively narrow, almost as narrow as the MAS signals and as expected for an isotropically rotating molecule in a liquid. By contrast, the spectrum of the static MCM-41 samples **a** and **b2** consists of a typical residual chemical shift anisotropy (CSA) signal pattern with axial symmetry, where the high field component is more intense than the low field component, in contrast to immobilized pyridine.<sup>29,42</sup> The corresponding spectrum of the static sample **c2** consists of a superposition of both types of signals, revealing the presence of two different slowly exchanging environments for hydrogen-bonded pyridine, one characterized by an isotropic and the other by an anisotropic reorientational diffusion.

In the case of an excess of pyridine, i.e., in the case of samples **c3** and **e3**, the  $^{15}\text{N}$  MAS spectra exhibit two pyridine signals of unequal intensities at lower fields, as depicted in Figure 6. These low field shifts are more pronounced for SBA-15 (sample **e3**) than for MCM-41 (sample **c3**). These shifts indicate that pyridine is rapidly exchanging between hydrogen-bonded surface sites and an inner non-hydrogen-bonded core phase, where the hydrogen bond sites are depleted as compared to low temperatures.

**Variable-Temperature  $^2\text{H}$  NMR Measurements.** To further analyze the anisotropic rotational motion of pyridine in mesoporous silica, we performed  $^2\text{H}$  NMR measurements on sample **e5** of MCM-41 loaded with pyridine- $4\text{-}d_1$ , which was prepared in such a way that less than a monolayer was occupied. The para-labeling was chosen, because the quadrupolar tensor of the para-position has the same principal axis system as the  $^{15}\text{N}$ -CSA tensor, due to the molecular  $C_{2v}$  symmetry.

The experimental and simulated  $^2\text{H}$  NMR spectra of this sample are depicted in Figure 7. Although the spectrum measured at 175 K exhibits a typical broad quadrupolar line shape, the high-temperature spectrum measured at 292 K is strongly narrowed. The quadrupolar coupling constants  $Q_{zz}$  and the asymmetry parameters  $\eta$  obtained from the simulations of the spectra are  $Q_{zz} = 129 \pm 3$  kHz and  $\eta = 0.05$  for the low-temperature spectrum and  $Q_{zz} = 10.8 \pm 1$  kHz and  $\eta = 0.3$  for the high-temperature spectrum.

## Discussion

The main results of the experiments described above can be summarized as follows.  $^{29}\text{Si}$  CPMAS shows that all materials



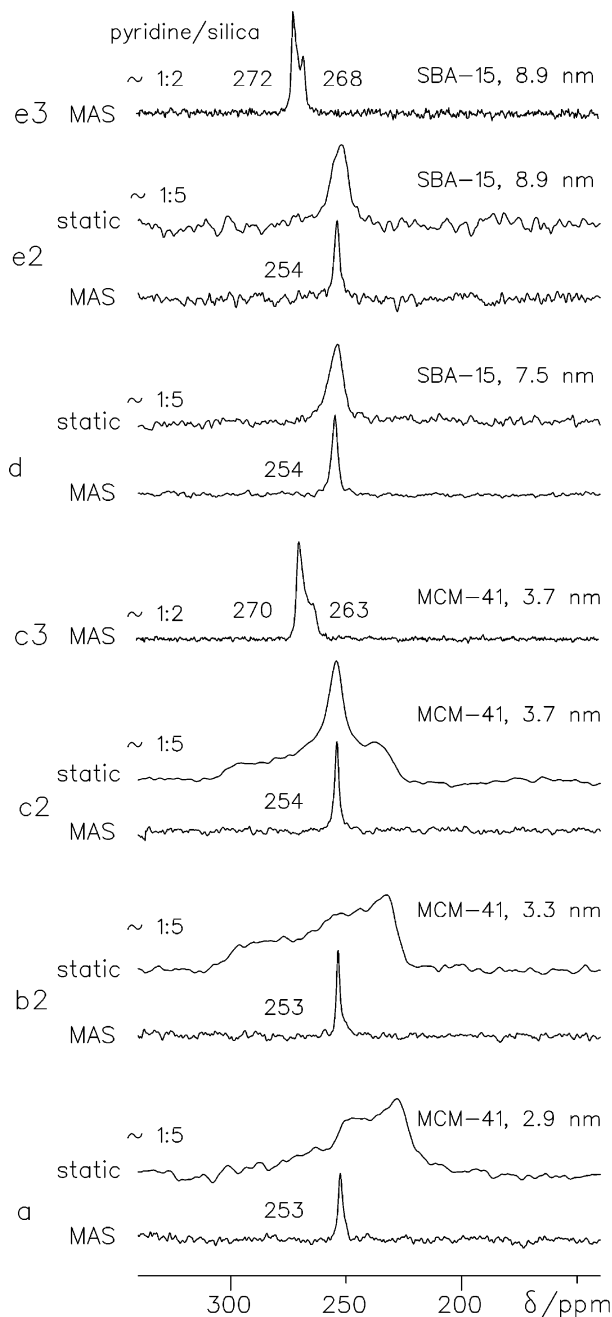


**Figure 6.**  $^{15}\text{N}\{^1\text{H}\}$  MAS (lower) and static (upper) spectra at room temperature of pyridine loaded onto the silica samples **a**, **b2**, **c2**, **d**, and **e2** and onto the same silica with an excess of pyridine **c3** and **e3**, respectively.

contain  $\text{Si}(\text{OH})$  groups  $\text{Q}^3$ . In addition, we find a substantial amount of geminal  $\text{Si}(\text{OH})_2$  groups  $\text{Q}^2$  in the materials with diameters of the cylindrical pores larger than 3–4 nm but not for those with smaller diameters.  $^1\text{H}$  MAS NMR shows that besides a small fraction, these silanol hydroxyl groups are of the “surface” type and can form hydrogen bonds with proton acceptors in the pores. By low-temperature  $^{15}\text{N}$  CPMAS NMR we find pyridine- $^{15}\text{N}$  exhibits in the regime of low coverage an isotropic  $^{15}\text{N}$  chemical shift of 251 ppm, corresponding to pyridine hydrogen bonded to surface OH groups. Excess bulk pyridine leads to a separate signal around 276 ppm, indicating that the slow hydrogen bond exchange regime is reached. Because the surface areas of the silica samples (Table 1) and relative amount of free and hydrogen-bonded pyridine (Figure 5, samples **c3** and **e3**) are known, we estimate that the maximum

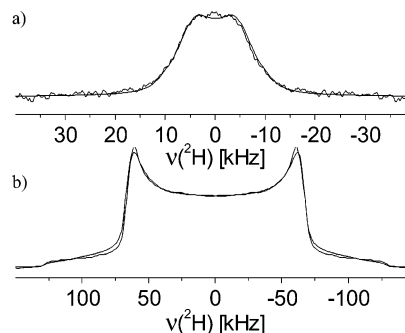


**Figure 7.** Experimental and simulated  $^2\text{H}$  NMR solid-echo spectra of pyridine-4- $d_1$  as guest in MCM-41, sample **c5**. Lower panel: the low-temperature (175 K) spectrum exhibits the full size and anisotropy of a quadrupolar  $-\text{CD}$  tensor. Upper panel: reduced quadrupolar line width due to the molecular motions of the pyridine on the silica surface. The simulation is performed employing the motional model described in the appendix and an  $-\text{SiOH}\cdots\text{N}$  angle of  $\alpha = (49 \pm 2)^\circ$ .

number of pyridine molecules on the surface  $n_{\text{OH}}$  is  $2.9 \pm 0.3 \text{ nm}^{-2}$  for MCM-41 silica (**c3**) and  $3.7 \pm 0.3 \text{ nm}^{-2}$  for SBA-15 silica (**e3**). These numbers were determined at 120 K. At room temperature we find that in the presence of an excess of pyridine the fraction of hydrogen-bonded pyridine is smaller, as compared to 120 K.

Static  $^{15}\text{N}$  NMR experiments at room temperature reveal a fast anisotropic reorientation of pyridine in MCM-41 but an isotropic reorientation in SBA-15. At low coverage of the surface, the isotropic  $^{15}\text{N}$  chemical shifts of pyridine are the same at low and at room temperature, indicating that at room temperature the motion of pyridine is such that it jumps from one silanol group to the other, corresponding to a surface diffusion process without leaving the surface.

In the following, we will discuss possible explanations for these findings, which will provide some interesting information concerning the structure of the inner surfaces of the materials studied, as well as the host–guest interactions and the guest molecule mobility.

**Properties of Surface Silanol–Pyridine Hydrogen Bonds and Silanol Solid-State Acidity of Mesoporous Silica.** Recently, some of us have succeeded in synthesizing solid 1:1 hydrogen-bonded complexes of 2,3,6-trimethylpyridine- $^{15}\text{N}$  (collidine- $^{15}\text{N}$ ) with carboxylic acids of varying strength, and in measuring the isotropic  $^1\text{H}$  and  $^{15}\text{N}$  and the anisotropic  $^{15}\text{N}$  chemical shifts as a function of the nitrogen–hydrogen distance measured by dipolar  $^2\text{H}$ – $^{15}\text{N}$  NMR.<sup>29</sup> Using the hydrogen bond correlation of Steiner between the distances  $r_{\text{OH}}$  and  $r_{\text{HN}}$  of NHO hydrogen bonds,<sup>43</sup>

$$p_{\text{OH}} + p_{\text{HN}} = 1 \quad p_{\text{OH}} = \exp\{-(r_{\text{OH}} - r_{\text{OH}}^0)/b_{\text{OH}}\} \\ p_{\text{HN}} = \exp\{-(r_{\text{HN}} - r_{\text{HN}}^0)/b_{\text{HN}}\} \quad (1)$$

where  $p_{\text{OH}}$  and  $p_{\text{HN}}$  represent the Pauling valence bond orders, and  $r_{\text{OH}}^0 = 0.942 \text{ \AA}$ ,  $r_{\text{HN}}^0 = 0.992 \text{ \AA}$ ,  $b_{\text{OH}} = 0.371 \text{ \AA}$ , and  $b_{\text{HN}} = 0.385 \text{ \AA}$  are empirical parameters derived by analysis of a series of neutron structures. We found the following expressions for the isotropic  $^1\text{H}$  and  $^{15}\text{N}$  chemical shifts of hydrogen-bonded complexes of collidine and pyridine with a variety of acids, i.e.

$$\delta(^{15}\text{N}) = \delta = \delta_{\text{HN}}^\infty - (\delta_{\text{HN}}^\infty - \delta_{\text{HN}}^0) \exp\{-(r_{\text{HN}} - r_{\text{HN}}^0)/b_{\text{HN}}\} \quad (2)$$

$$\delta(^1\text{H}) = \delta = 4\Delta_{\text{H}} p_{\text{OH}} p_{\text{HN}} + \delta_{\text{OH}}^0 p_{\text{OH}} + \delta_{\text{HN}}^0 p_{\text{HN}} \quad (3)$$

In these equations,  $\delta_{\text{HN}}^\infty = 268 \text{ ppm}$  for non-hydrogen-bonded

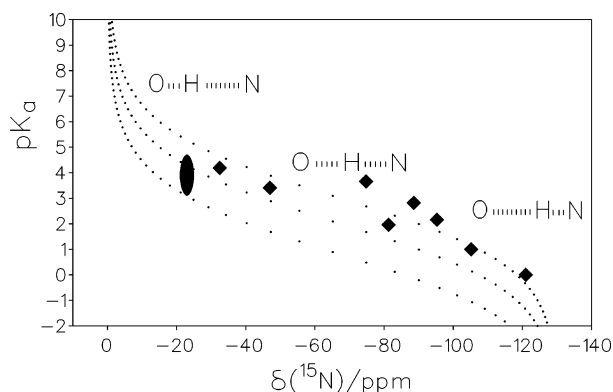


**Figure 8.** Correlation of  $pK_a$  values of acids AH in solid-state complexes with bases. The upper dotted curve corresponds to eq 4. The routes correspond to collidine–acid complexes described in ref 29. For the two lower curves the intercept was reduced to 1.8 and 0.8, respectively. The solid ellipsoid corresponds to mesoporous silica, both of the MCM-41 and the SBA-15 type. For further explanations see text.

collidine and 276 ppm for pyridine, and  $(\delta_{\text{HN}}^\infty - \delta_{\text{HN}}^0) = 130$  ppm.  $\delta_{\text{OH}}^0$  and  $\delta_{\text{HN}}^0$  are the fictitious limiting  $^1\text{H}$  chemical shifts of the isolated OH and NH groups, where the values  $\Delta_{\text{H}} = 16.7$  ppm,  $\delta_{\text{OH}}^0 = 1$  ppm, and  $\delta_{\text{HN}}^0 = 7$  ppm were obtained by comparison with the experiment.<sup>29</sup>

Using eq 2, we obtain an average distance of  $r_{\text{HN}} = 1.68$  Å for pyridine hydrogen bonded to silanol groups and the corresponding distances  $r_{\text{OH}} = 1.01$  Å or  $r_{\text{ON}} = 2.69$  Å assuming a linear NHO hydrogen bond. Equation 3 predicts for these values a  $^1\text{H}$  chemical shift of about 10 ppm, which is in excellent agreement with the experimental findings of Figure 4. We note that this is the first time that hydrogen bond geometries in disordered systems have been estimated from isotropic NMR chemical shifts.

We note that the pyridine chemical shifts are the same for both the MCM-41 and SBA-15 materials, and independent of the pore size. Hence, the same is true for the hydrogen bond geometries. The silanol groups are not able to protonate pyridine, a result that corroborates earlier IR measurements<sup>18</sup> and ab initio calculations.<sup>44</sup>

In ref 29 we were also able to obtain a correlation of the  $pK_a$  values of the acids AH in the solid-state complexes with collidine with the  $^{15}\text{N}$  chemical shift of the latter as illustrated by the upper curve of Figure 8, generated using the equation

$$pK_a = -3.5(r_{\text{OH}} - r_{\text{HN}}) + 2.8 \quad (4)$$

in combination with eqs 1–3. To form a quasi-symmetric complex in the solid state with  $r_{\text{OH}} \approx r_{\text{HN}}$ , an acid is needed which exhibits a  $pK_a$  value of 2.8. This value is much smaller than the  $pK_a$  value of 7.43 in water.<sup>45</sup> This difference arises from the very small dielectric constant in the organic solid state as compared to water.

Equation 4 is not directly valid for pyridine, whose protonated form exhibits a  $pK_a$  value of 5.25.<sup>45</sup> In other words, because pyridine is less basic than collidine, a stronger acid is required in the solid state to produce a quasi-symmetric complex with pyridine. Unfortunately, we do not know the  $pK_a$  value of such an acid, but the difference of the  $pK_a$  values of pyridine and collidine indicate that this value may be reduced by up to 2  $pK_a$  units. Assuming similar  $^{15}\text{N}$  chemical shift parameters, we estimate the two lower dotted curves in Figure 8. Using the chemical shift of 251 ppm for pyridine hydrogen bonded to silanol groups, which is  $-24$  ppm high field from free pyridine

absorbing at 276 ppm with respect to solid ammonium chloride, we estimate a  $pK_a$  value of the silanol groups of about 4 or lower, as indicated by the solid ellipsoid in Figure 8. This means that the geometry of the silanol–pyridine hydrogen bonds in mesoporous silica is similar to a hypothetical hydrogen bond of an acid—exhibiting a  $pK_a$  of 4 in water—with pyridine in an environment of a low dielectric constant. This value is substantially smaller than the first  $pK_a$  value of 9.9 published for  $\text{H}_4\text{SiO}_4$  at 30 °C<sup>45</sup> and the value of 11 found for  $(\text{CH}_3\text{O})_3\text{SiOH}$ .<sup>46</sup> By comparison of silica–acetone complexes in  $\text{CCl}_4$  with those of phenol with acetone, values of 7.5 have been estimated.<sup>47</sup>

**Number of Surface SiOH Groups.** As mentioned in the Introduction, using IR spectroscopy of pyridine in mesoporous silica, values of  $0.5\text{--}0.6\text{ nm}^{-2}$  have been estimated for the number of pyridine molecules  $n_{\text{pyr}}$  involved in hydrogen bonds with silanol groups in the inner surfaces of MCM-41 samples.<sup>18</sup> On the other hand, the surface covered by silyl groups varies from  $0.74$  to  $1.85\text{ nm}^{-2}$ ,<sup>16</sup> whereas the number of silanol groups  $n_{\text{OH}}$ , as determined by  $^{29}\text{Si}$  CP NMR, varies between 2.5 and  $3.0\text{ nm}^{-2}$ .<sup>17</sup> In normal amorphous silica usually values of about  $5\text{ nm}^{-2}$  are observed.<sup>20</sup> The question why lower values are obtained for mesoporous silica materials is, therefore, still unsolved.

The values of  $3\text{ nm}^{-2}$  in the case of MCM-41 and of  $3.7\text{ nm}^{-2}$  in the case of SBA-15 obtained in this study by  $^{15}\text{N}$  NMR of pyridine correspond also to  $n_{\text{pyr}}$ . Most of the silanol groups detected by  $^1\text{H}$  MAS NMR were able to form hydrogen bonds to added pyridine. Thus, there are only few silanol groups hidden in the walls, interacting with each other in such a way that they cannot form hydrogen bonds to pyridine. We offer the following interpretation of the different findings for the values of  $n_{\text{pyr}}$  by  $^{15}\text{N}$  NMR and IR. We performed our experiments at 120 K, where for NMR the slow hydrogen bond exchange regime is reached, as found by the occurrence of two  $^{15}\text{N}$  signals for hydrogen-bonded and non-hydrogen-bonded pyridine in the core of the pores. As depicted in Figure 5, the interpretation that the former occurs from hydrogen bonding to surface OH groups was corroborated by the finding that the core peak of pyridine not hydrogen bonded to the surface groups was shifted to high field by the addition of water. Now, also the core pyridine molecules are involved in hydrogen bonding; preliminary experiments outside mesoporous silica give evidence for pyridine–water complexes.

In contrast, IR measurements on pyridine in mesoporous silica were performed at room or even higher temperature.<sup>18</sup> Here, we find that when pyridine is used as a probe for the number of the surface silanol groups, attention has to be paid to the temperature where this measurement is done. Evidence for this interpretation is based on the finding that the  $^{15}\text{N}$  chemical shift of pyridine is the same at low and at room temperature in the absence of an excess of pyridine (Figures 5 and 6). Thus, in this regime all pyridine molecules are hydrogen bonded to the surface silanol groups at low and at room temperature. In the case of an excess of pyridine, separate lines for non-hydrogen-bonded pyridine and hydrogen-bonded pyridine are observed at low temperatures. It is, therefore, surprising, that the room-temperature pyridine signal averaged over both environments appears at lower field than the predicted shift on the basis of the relative intensities of bound and free pyridine at 120 K. We associate this effect with an increased entropy of pyridine in a “bulk” liquid phase inside the pores as compared to the surface sites. Therefore, at room temperature, the number of pyridine molecules  $n_{\text{pyr}}$  hydrogen bonded to the surface is smaller than the number of silanol groups. We note that this



effect is more pronounced for SBA-15 exhibiting larger pores than MCM-41 (samples **c3** and **e3** in Figure 6). Moreover, the signals are split into two resolved singlets with unequal intensity. We offer the following explanation for this finding. We assign the peak at lower field to pyridine in pores or pore areas that are almost completely filled, and the peak at higher field to pores or pore areas that are partially filled; hence, in the latter the fraction of H-bonded pyridine is slightly higher as compared to the former. This interpretation also explains why the shifts are smaller in the case of MCM-41.

At room temperature, as discussed in detail below, the pyridine molecules jump very rapidly in the NMR time scale from one silanol group to the other, during which they perform an anisotropic rotational diffusion coupled to a surface translational diffusion in mesoporous silica exhibiting pore diameters below 3 nm. In the materials with larger pores the rotational diffusion is isotropic. We note that this result is not in agreement with a recent study reporting that desorption energies of pyridine adsorbed on  $Q^3$  and  $Q^2$  species of MCM-41 silica are quite different, i.e., 91.4 and 52.2 kJ mol<sup>-1</sup>, respectively.<sup>17</sup> Our results indicate a fast hydrogen bond exchange of pyridine with the different types of silanol groups which should lead to a single activation energy for desorption.

**Modeling of the Inner Surfaces of Mesoporous Silica Exhibiting Cylindrical Pores.** To discuss the motions of pyridine in mesoporous silica in further detail, it is desirable to have a picture of the inner surface structure of mesoporous silica, taking into account the new experimental results. As mentioned in the Introduction, both silica materials consist of a silicon dioxide tetrahedron network, forming a 2-dimensionally hexagonal array of cylindrical pores. Whereas the pore diameters are 2.9–3.7 and 7.5–8.9 nm, respectively, the pore to pore distances are in the range 4.0–4.9 and 10.4–11.1, respectively, for the samples of MCM-41 and SBA-15. Thus the pore walls have a mean thickness of only 1.2 nm for MCM-41 and 2.2 nm for SBA-15 materials investigated in our work.

A first approach to describe the surfaces of mesoporous silica is to start by an analysis of the unit cell surfaces of various crystal modifications of SiO<sub>2</sub>. When the dangling bonds of Si are saturated with OH groups, and those of O with H, one finds  $n_{OH}$  values for cristobalite and tridymite of about 4.5–4.6 nm<sup>-2</sup> for the surfaces with Si(OH) silicon atoms of the  $Q^3$  type.<sup>48</sup> Naturally, the number is about twice as much larger for surfaces containing Si(OH)<sub>2</sub> groups. As an example, we depict in Figure 9a a fragment of tridymite,<sup>49</sup> consisting of six-membered Si rings in a chair configuration, in a perspective view normal to the (010) plane. Here, each ring contributes three axial SiOH groups  $Q^3$  to the surface, separated by a single  $Q^3$  silicon. As each  $Q^3$  is part of three tridymite ring fragments, each fragment contributes only a single axial SiOH group to the surface. Each six-membered ring exhibiting Si–Si distances of about 3.1 Å and O–Si–O angle of 109° covers a neat surface of about 0.22 nm<sup>2</sup>, leading to a value of  $n_{OH} \approx 4.5$  nm<sup>-2</sup>, as reported by De Boer.<sup>48</sup> By checking a number of different crystal structures of SiO<sub>2</sub><sup>50</sup> we could confirm the validity of these numbers. We note that Si(OH)<sub>3</sub> groups  $Q^1$  occur only in corners.

To model the interaction of ammonia with silica surfaces exhibiting silanol concentrations of  $n_{OH} \approx 2$  nm<sup>-2</sup>, Civalleri and Ugliengo<sup>22</sup> have explored an ordered planar surface derived from the aluminosilicate edingtonite, where a fragment is depicted in Figure 9b. Here, each SiOH group of the surface is separated by two rather than one silicon atoms of the  $Q^4$  type. A cylindrical model surface with a smaller number of  $n_{OH} \approx 1.2$  nm<sup>-2</sup> was proposed by Jentys et al.<sup>18</sup> to accommodate a corresponding

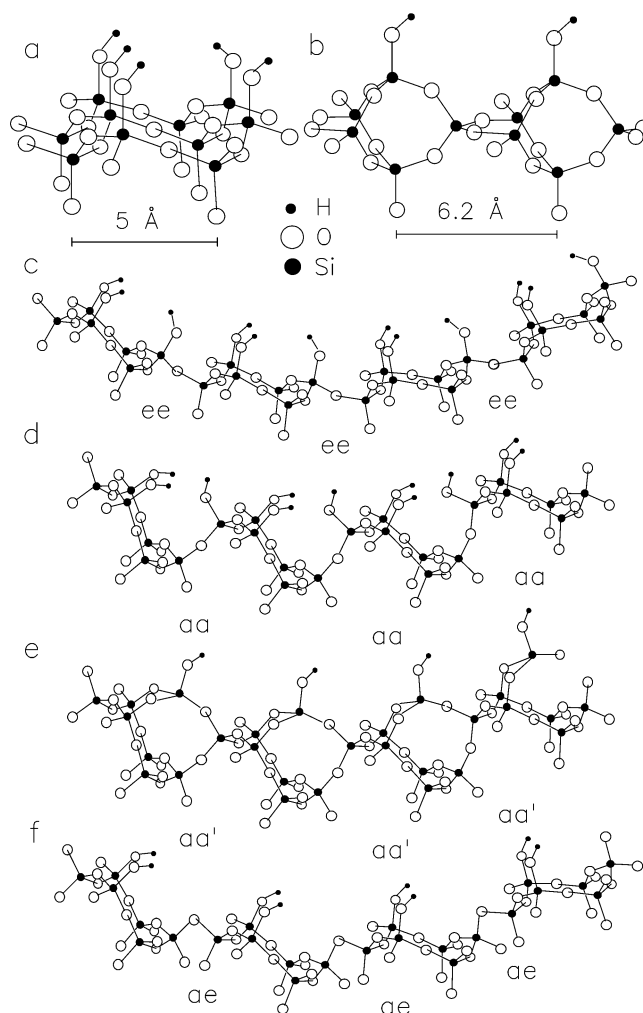


**Figure 9.** Low-molecular weight fragments of silica. (a) Fused double fragment derived from the unit cell of tridymite, perspective view normal to the (010) plane.<sup>49</sup> Half of the Si atoms in the surface are of the  $Q^3$  type, i.e., contain a single OH group. (b) Single fragment of edingtonite.<sup>22</sup> Only one-third of the surface silicon atoms are of the  $Q^3$  type. (c) and (d) Tetrameric tridymite fragments linked by equatorial–equatorial (ee) and axial–axial (aa) connections. (e) Tetrameric fragment obtained from the fragment (d) by incorporation of additional silicon units, aa'. (f) Tetrameric fragment linked by ae connections.

value for the interaction of pyridine with MCM-41 studied by IR spectroscopy. Spohr et al.<sup>51</sup> have proposed a surface that was obtained by cutting out a cylindrical cavity from a previously simulated configuration of vitreous silica, with  $n_{OH} \approx 2.5$  nm<sup>-2</sup>. The OH groups were found to be irregularly clustered in certain surface regions, whereas other regions did not contain any OH groups, but only  $Q^4$  silicon atoms with highly deformed Si–O bond angles. An inspection of this surface shows<sup>52</sup> that the axes of many OH groups are located in the surface, rather than pointing into the pore center.

A description of the mesoporous silica materials in terms of perforated crystalline or amorphous silica seems, therefore, unlikely. More correct appears a silica network that starts to grow at the TEOS-solution/copolymer-precursor interface, forming first domains of monolayers of silica around the copolymer rods. These monolayers may be stabilized by Coulomb interactions between  $C_nTA^+$  and  $SiO_4^{4-}$ . Then the interstitial space is filled, connecting the different domains. Though, on the average, particles of MCM-41 and SBA-15 have no periodic structure on the atomic length scale, they are believed to consist of local domains that resemble the known crystal structures.

Inspired by the previous proposals for mesoporous silica surfaces, we propose in the following a cartoon that naturally explains the occurrence of a wide range of silanol concentrations  $n_{\text{OH}}$ . We start from the six-membered tridymite surface fragments of Figure 9a. In Figure 9c they are combined by equatorial–equatorial (ee) links and slightly bent to an arc that may be completed to a circle and to a cylindrical fragment. We estimate that  $n_{\text{OH}}$  will be similar to the value for the planar surface, i.e.,  $4.5 \text{ nm}^{-2}$  because a given pair of silanol groups  $\text{Q}^3$  is separated by a single  $\text{Q}^4$  silicon. By curiosity, we combined then the same fragments by axial–axial (aa) links, corresponding to another way of cutting a tridymite crystal, leading to the arc depicted in Figure 9d. Surprisingly, we still obtain  $\text{Q}^3$  silicon atoms, but a pair of  $\text{Q}^3$  silicon atoms is now separated either by zero or by two silicon atoms of the  $\text{Q}^4$  type. It seems that the OH groups are able to interact with each other and form surface hydrogen bonds according to Figure 1d. The number of OH groups per tridymite fragment is the same as for the ee-combination, but the contribution of a single fragment to the surface area has decreased. Therefore,  $n_{\text{OH}}$  increases somewhat as compared to the ee combination. It is tempting to assign the interacting silanol groups of the aa combination to the silanol groups in the  $3400\text{--}3600 \text{ cm}^{-1}$  wavenumber region, which are red-shifted from those of the isolated silanol groups ( $3745 \text{ cm}^{-1}$ ).<sup>18</sup> As the ratio of the two types of silanol groups depends on the sample preparation, we looked at how we could decrease the number of silanol groups. One possibility is depicted in Figure 9e, where we assume that an additional silicon atom is introduced, replacing 3 silanol groups by a single one. We label this modified combination as aa'. We obtain a similar surface as the edingtonite surface of Figure 9b, exhibiting a similar value of  $n_{\text{OH}} \approx 2 \text{ nm}^{-2}$ . The difference is that each  $\text{Q}^3$  silicon is now part of a five-membered instead of a four-membered Si ring, leading to a curved rather than a planar surface. Finally, in Figure 9f we have depicted an arc constructed by axial–equatorial (ae) links, which leads to the suppression of one-third of the surface silanol groups. However, the ae-links probably introduce a substantial steric strain and might, therefore, not be realistic.

In Figure 10 we have prepared a cartoon of a pore exhibiting a diameter of about 3–4 nm, as found for the MCM-41 material. The ring consists of 18 tridymite units of the type  $(\text{aa}'\text{--aa}'\text{--ee--aa}'\text{--aa--ee--aa}'\text{--aa}'\text{--ee})_2$ , exhibiting a hexagonal profile. Only SiOH but no  $\text{Si}(\text{OH})_2$  groups are present. We estimate that the number of silanol groups is around  $3 \text{ nm}^{-2}$ . The Si–O axis of the  $\text{Q}^3$  silicon atoms are arranged fairly well but not perfectly in a perpendicular way with respect to the surface, in a similar way as in the cartoon of Figure 1c. Pyridine molecules are added at low coverage and form hydrogen bonds with the SiOH groups. In a given hydrogen bond, the pyridine rings can in principle rotate around the  $\text{O--H}\cdots\text{N}$  axes, and around the Si–O axes. Furthermore, the pyridine rings can jump from one hydrogen bond to another. We note that the  $\text{O--H}\cdots\text{N}$  axis is not distributed in all possible orientations of space. In particular, it seems that OH directions parallel to the cylindrical pore axis are absent. This feature will explain later the anisotropic reorientation of pyridine in MCM-41.

As the reorientation is isotropic for a pyridine surface diffusion in SBA-15, we tried to incorporate this feature into a model for SBA-15 exhibiting much larger pore diameters, as described in the following. In Figure 11 we arbitrarily consider the hexagonal tridymite sequence  $(\text{ee--aa}'\text{--ee--aa}'\text{--ee--aa}')_6$ . This ring alone would exhibit only surface–Si(OH) groups but no geminal  $\text{Si}(\text{OH})_2$  groups found here experimentally for SBA-

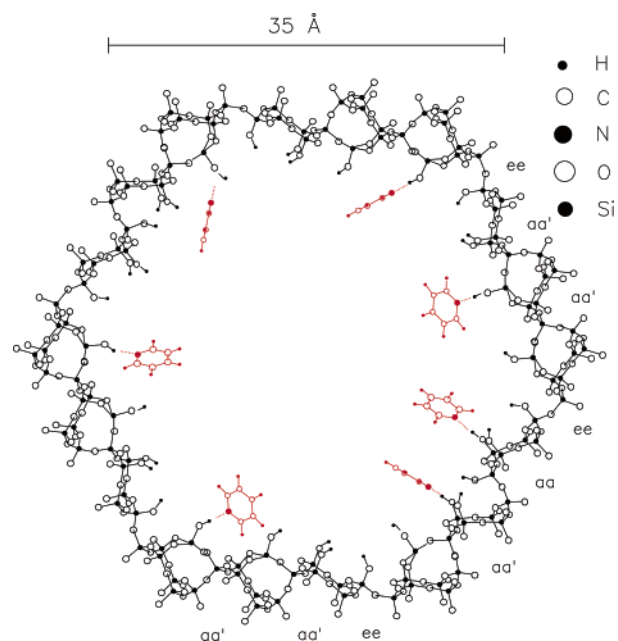


**Figure 10.** Cyclic hexagonal ring consisting of four fragments  $\text{aa}'\text{--aa}'\text{--ee--}$  and two fragments  $\text{aa}'\text{--aa--ee--}$ . By fusion of several rings a cylindrical model pore is obtained, exhibiting features found experimentally for MCM-41. The surface contains only SiOH groups  $\text{Q}^3$ , which can form hydrogen bonds with added pyridine. Silanol groups  $\text{Q}^3$  can be separated by zero, one, or more silicons of the  $\text{Q}^4$  type. As the orientation of the silanol OH groups is not evenly distributed in all directions of space the motion of pyridine will be anisotropic as described below.

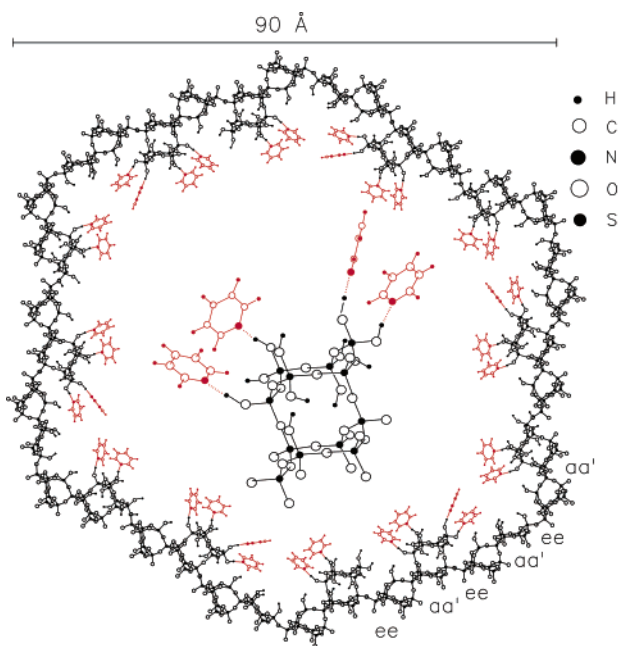


**Figure 11.** Circle of six tridymite units  $(\text{ee--aa}'\text{--ee--aa}'\text{--ee--aa}')_6$ . After fusion of several rings a model pore is obtained exhibiting experimental features of SBA-15. The surface is decorated with additional single tridymite fragments as “surface defects”. The defects contain now isolated SiOH groups  $\text{Q}^3$  in equatorial position as well as geminal  $\text{Si}(\text{OH})_2$  groups  $\text{Q}^2$ , where one OH group is in equatorial and the other in axial position. The distribution of the OH groups and hence the reorientation of pyridine is now isotropic.

15. Therefore, we decorated each inner side of the hexagon arbitrarily with two tridymite fragments as defects or “isles”. As illustrated in the insert, we create in this way six new equatorial surface OH groups in addition to the three axial OH

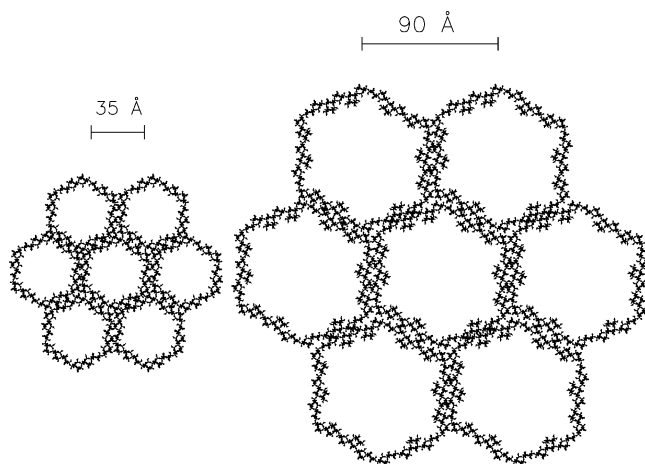


**Figure 12.** Hexagonal arrays of the rings depicted in Figures 10 and 11.

groups, or three  $Q^3$  with equatorial OH groups and three  $Q^2$  with geminal OH groups. Now, pyridine will find not only axial but also equatorial hydrogen bonding sites, which will lead eventually to an isotropic reorientational diffusion. The introduction of such defects increases the number  $n_{OH}$ , which is also in agreement with the experimental value of  $3.7 \text{ nm}^{-2}$  for SBA-15 material.

In Figure 12 we have assembled the rings of Figures 10 and 11 to mimic arrays of MCM-41 and SBA-15. In this model, it is seen that the inner surface of SBA-15 is substantially “rougher” than the surface of MCM-41. It would be more appropriate to speak of a disordered porous interface in the case of SBA-15 rather than of a surface. Thus, the walls of SBA-15 are to a substantial amount composed by this interface.

**Molecular Motions of Pyridine in Mesoporous Silica.** From the model surfaces of Figures 10–12 we can now derive several degrees of freedom of the molecular motions of pyridine bound to the inner surfaces of mesoporous silica by hydrogen bonding, whose combination eventually leads to a coupled rotational and translational surface diffusion. We remember that rotational diffusion is anisotropic in the case of the silica samples with the smaller pore diameters but becomes isotropic when the diameters are increased.

Figure 13a depicts a rotation of pyridine around the Si–O axis of a  $Q^3$  unit, which is axially placed with respect to the surface. In Figure 13b is depicted a rotation of pyridine around the NHO axis. OHN hydrogen bond jumps are depicted in Figure 13c,d. The former corresponds to a jump between two axial  $Q^3$  units, whereas the latter corresponds to a jump between an axial  $Q^3$  unit and an equatorial  $Q^3$  or  $Q^2$  unit.

We note that for a planar surface a  $180^\circ$  rotation about the Si–O axis and an axial–axial NHO hydrogen bond jump are equivalent with respect to the reorientation in an external magnetic field. In a cylindrical surface the surface diffusion process is furthermore associated with an anisotropic reorientation of pyridine with respect to the external field, as illustrated in Figure 14. This is because an axial–axial NHO-hydrogen bond jump is no longer equivalent to an  $180^\circ$  Si–O-rotation. The combined motions of a Si–O-rotation and a NHO hydrogen bond jump leads to the two-dimensional diffusion of pyridine in the surface.

**Anisotropy of the Guest Molecule Motion and Surface Geometry of the Silica.** The question now arises whether one can understand the different types of the reorientation of pyridine in SBA-15 and MCM-41 in terms of the above models. In principle, there are two limiting cases for the motion of pyridine

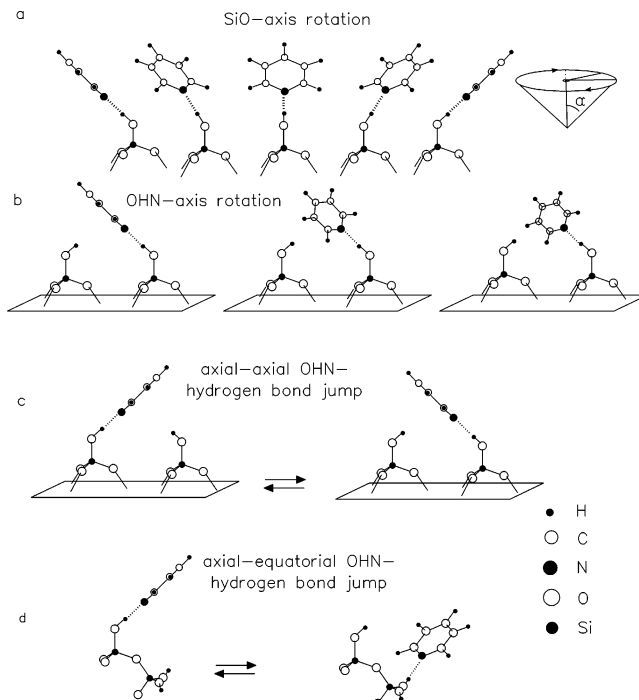


**Figure 13.** Possible motions of pyridine hydrogen bonded to a planar silica surface.

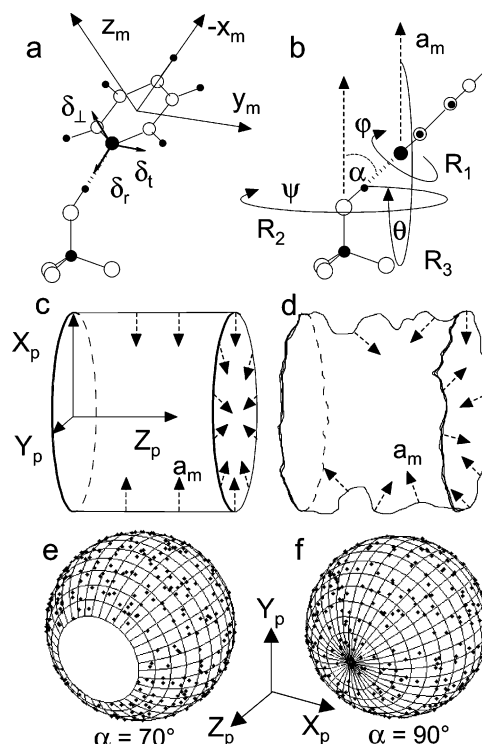


**Figure 14.** Simplified model for the simulation of the reduced  $^{15}\text{N}$  CSA pattern of pyridine in MCM-41 at room temperature.

in mesoporous silica: (i) the pyridine molecules jump practically directly from one surface OH group to the next, without spending an appreciable time in a liquid or inner bulk phase; (ii) the molecules jump from the surface into a liquid or inner bulk phase, where they stay some time before jumping to the next surface OH group. As already mentioned, this question can be answered by comparing the room temperature to the low-temperature  $^{15}\text{N}$  MAS spectra. As long as an excess of pyridine is avoided, there is only a slight shift, less than 3 ppm to low-field, of the  $^{15}\text{N}$  signal. This indicates that the adsorbed



molecules spend most of their time on the surface and do not leave the surface for an appreciable fraction of time. Thus the motion of the pyridine molecules is a surface diffusion or a migration on the surface. This finding is in agreement with a reduced diffusion coefficient of pyridine in mesoporous silica, as compared to bulk pyridine.<sup>31</sup>

Further information about the surface diffusion can be obtained from the static room-temperature <sup>15</sup>N NMR spectra. In the case of the MCM-41 a reduced axially symmetric CSA pattern is observed, where the reduction factor is about -7.7 with respect to bulk pyridine or +4.5 relative to pyridinium.<sup>42</sup> By contrast, in the case of SBA-15, within the margin of error, a fully isotropic <sup>15</sup>N line is observed at room temperature.

Unfortunately, models of Figures 10 and 11 are arbitrary and many variations are possible. Therefore, to reproduce the <sup>15</sup>N and <sup>2</sup>H NMR spectra of the static samples, we used the simplified model depicted in Figure 14; for a detailed discussion, see the Appendix. The silica pores are so large that it can be assumed that an adsorbed pyridine molecule remains in the same pore longer than the time scale of the NMR experiment. Let us define the pore direction as the Z axis of the coordinate system and denote the orientation of the pyridine molecule by the angles  $\psi$  and  $\theta$  (Figure 14). In the case of an idealized homogeneous smooth surface, Figure 14b, all values of these angles have the same probability. At room temperature the anisotropy of the pyridine CSA tensor will be reduced by the combined fast rotational and translational diffusion on the surface. From Figure 14c it is evident that the angle  $\alpha$  may not take all possible values, due to the orientational constraints. The situation is different if the surface exhibits a substantial roughness (Figure 14d). In this situation all values of the angle  $\alpha$  is possible, resulting in the fast limit in a full averaging of the anisotropy. In other words the anisotropy of the static line is a measure for the surface smoothness. This model is corroborated by the following observations in by <sup>29</sup>Si-CPMAS NMR (Figure 3): in sample **b1** almost no surface =Si-(OH)<sub>2</sub> groups are detected, whereas in sample **c1** some surface =Si-(OH)<sub>2</sub> groups are present and in sample **e1** an appreciable amount of surface =Si-(OH)<sub>2</sub> groups are visible. These surface =Si-(OH)<sub>2</sub> groups are effectively defects in the surface homogeneity and thus the smoothness. Consequently, the roughness of the silica surfaces increases strongly from sample **b1** to sample **e1**, which coincides with a reduction of the anisotropy of the <sup>15</sup>N NMR signals. The low concentration of the =Si-(OH)<sub>2</sub> groups on the surface of the MCM-41 silica samples (Figure 3, **b1** and **c1**) and the presence of the anisotropic signal in the static spectra obtained for these silica (Figure 6 **a-c2**) means that in these samples the inner pore surface is homogeneous to a high degree. By contrast, the SBA-15 silica sample shows a high concentration of the =Si-(OH)<sub>2</sub> groups (Figure 3, **e1**) and the absence of the anisotropic component in the room-temperature <sup>15</sup>N NMR static spectra (Figure 6, **d** and **e2**) and, consequently, has plenty of surface defects, i.e., a considerable roughness.

As discussed above, the <sup>15</sup>N line shape of pyridine depends on the rotational state of the pyridine molecule. This implies that it is possible to reconstruct this information from the line shape. This gives us the unique chance to study the dynamics of the adsorbed molecules on a quantitative level, which is unachievable for silica gels without this high degree of surface homogeneity and ordering. There is no unambiguous relationship between the 1D NMR line shape and the motion. Thus it is necessary to make a model of the rotational motion, calculate the corresponding line shape, and compare this with the experimentally found shape. For this calculation, two types of infor-

**TABLE 2: Principal Components of the Chemical Shift Tensor for Some Pyridine Derivatives**

| compound               | $\delta_{\text{iso}}/\text{ppm}$ | $\delta_r/\text{ppm}$ | $\delta_t/\text{ppm}$ | $\delta_{\perp}/\text{ppm}$ | lit.      |
|------------------------|----------------------------------|-----------------------|-----------------------|-----------------------------|-----------|
| collidine              | 268                              | 490                   | 345                   | -30                         | ref 29    |
| collidine-benzoic acid | 234                              | 403                   | 323                   | -30                         | ref 29    |
| collidinium            | 148                              | 155                   | 275                   | 13                          | ref 29    |
| pyridine               | 278                              | 541                   | 374                   | -81                         | ref 42    |
| pyridine...HO          | 251                              | 475                   | 360                   | -80                         | estimated |
| pyridinium             | 172                              | 244                   | 311                   | -40                         | ref 42    |

<sup>a</sup> Collidine  $\equiv$  2,4,6-trimethylpyridine. All values are referenced to <sup>15</sup>NH<sub>4</sub>Cl.

mation are necessary, namely, the values of the static tensor and a model of the rotation. In principle, it is possible to gain the tensor values directly from static low-temperature <sup>15</sup>N NMR experiments. However, due to the low signal-to-noise ratio of the <sup>15</sup>N spectra, which is a result of the sample size and the necessary restrictions of the amount of pyridine in the pores, we were not able to obtain suitable low-temperature <sup>15</sup>N static spectra experimentally. Therefore, the principal values of the pyridine chemical shift anisotropy (CSA) tensor have to be estimated.

One of the principal CSA axes is the molecular symmetry axis, which is defined as the NC<sub>4</sub> axis, the second axis is the normal of the molecular plane, and the third one bisects the C<sub>2</sub>-C<sub>3</sub> and C<sub>5</sub>-C<sub>6</sub> bonds (Figure 14a). The corresponding principal values are called  $\delta_r$ ,  $\delta_{\perp}$ , and  $\delta_t$  in the following. The hydrogen bond causes a well-pronounced high-field shift of the  $\delta_t$  component and weak shifts of the  $\delta_r$  and  $\delta_{\perp}$  components toward high and low fields, respectively. In ref 29 it was shown that the <sup>15</sup>N chemical shift is strongly correlated to the geometry of a hydrogen bond and a direct correlation was established for solid 1:1 pyridine derivative-acid complexes. Table 2 collects data of the <sup>15</sup>N CSA tensors of a number of pyridine derivatives. It is evident that there is a similar correlation and the formation of the hydrogen bond changes their tensors in the same way. Estimation of the CSA tensor components for the pyridine molecules involved in the hydrogen bonding can be done in the following way. First, changes of the 2,4,6-trimethylpyridine CSA tensor components caused by formation of the 1.68 Å hydrogen bond compare to the tensor of a nonbonded molecule are calculated using the correlation obtained in ref 29. It is now possible to extrapolate these data on a pyridine molecule involved in the hydrogen bonding of the same length to get the needed tensor because the values of bulk pyridine CSA tensor components are known, Table 2. The simulated <sup>15</sup>N NMR static spectra for bulk pyridine and the pyridine involved in the hydrogen bonding with the surface hydroxyl groups are depicted in Figure 15a,b, respectively.

At room temperature a motional averaged axial symmetric <sup>15</sup>N CSA tensor with  $\sigma_{11} = 300$  and  $\sigma_{22} = \sigma_{33} = 230$  ppm is observed (Figure 15f). In the following we want to interpret this averaging by a suitable motional model. In principle, the following dynamic processes have to be taken into account: (i) rotation of pyridine around the molecular C<sub>2</sub> axis; (ii) nutation of the O-H...N hydrogen bridge around the Si-O bond with a constant Si-O-H angle ( $\pi - \alpha$ ), assuming that the hydrogen bond is linear; (iii) migration of the pyridine molecules along the surface (Figures 13a-d). All these processes are assumed to be independent of each other.

The question now arises, which of these processes contributes to the experimentally found line shape? Assuming that all three processes are fast on the NMR time scale, the following averaging is obtained. The rotation around the molecular C<sub>2</sub>

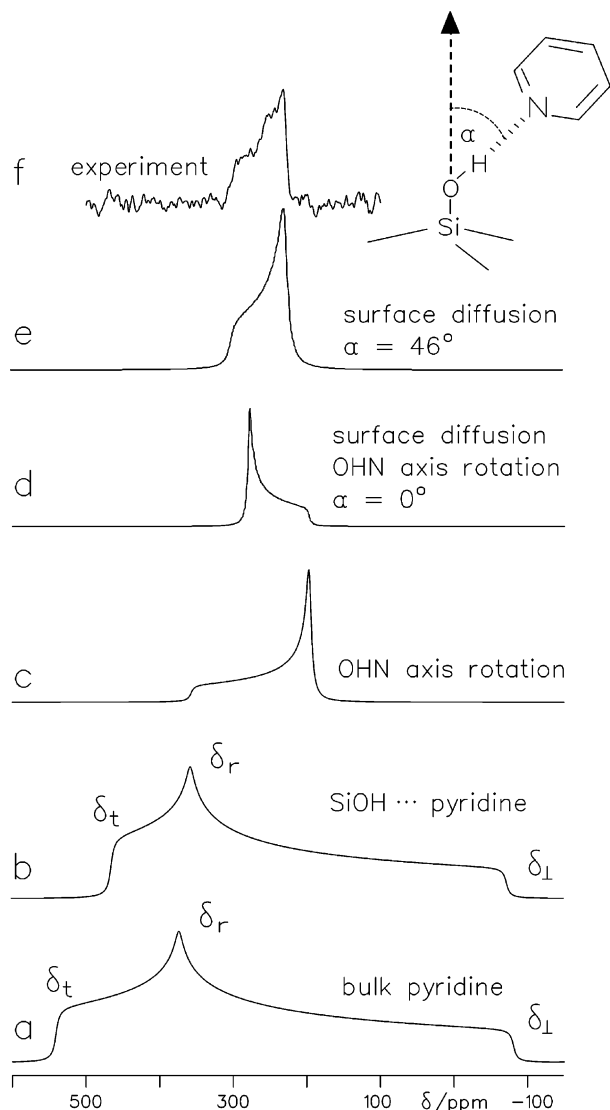


**Figure 15.** Simulation of the solid state NMR spectra of a pyridine molecule under different conditions. The bulk pyridine (a) and a weekly hydrogen-bonded pyridine (b). Modulation of the chemical shift anisotropy (CSA) Tensor of the hydrogen-bonded pyridine by its fast rotation along  $C_2$  axis only (c) and including its dynamic on the surface with angle  $\alpha = 0^\circ$  (d). The same tensor if the fast rotation along  $C_2$  axis is frozen and angle  $\alpha = 46^\circ$  (e). Experimental spectra of pyridine loaded onto the silica sample **b2** (f).

axis changes the tensor to an axial symmetry, with the principal components  $\sigma_{11} = 357$  ppm and  $\sigma_{22} = \sigma_{33} = 197.5$  ppm (Figure 15c). The effect of the migration along the surface reduces the tensor anisotropy and changes its sign (Figure 15d). The nutation around the Si–O bond causes a further line narrowing. The Si–O–H angle, the angle  $(\pi - \alpha)$  in our model, should be of the order 110–140 degrees. However, in this case the tensor anisotropy is almost 0, which is in contradiction to the experiment. Thus, this model, depicted in Figure 13a–c, cannot reproduce the experimental spectra. We can conclude that not all three processes contribute to the line shape, i.e., at least one of the three motional modes is not in the fast NMR limit. It is reasonable to assume that there are strong steric hindrances for the free rotation of the pyridine molecule around the molecular  $C_2$  axis. In this situation the ring will orient parallel to the surface, Figure 13a. Calculating this model yields a very good agreement between the experimental and the calculated  $^{15}\text{N}$  spectrum for the angle  $\alpha = 46 \pm 2^\circ$  (Figure 15e).

Further evidence for this model is taken from the  $^2\text{H}$  NMR spectra displayed in Figure 7. Simulating the fast exchange spectrum displayed in Figure 7a employing this motional model is in perfect agreement with the experimental spectrum for a jump angle of  $\alpha = 49 \pm 2^\circ$ . Thus the observed line shape is the direct result of the quasi two-dimensional motion of the pyridine molecules on the surface, combined with the rotation around the –SiO bond. We wish to note that in principle it is possible to prove this model by two-dimensional exchange NMR spectroscopy. Due to the very low concentration of pyridine inside the mesopores such an experiment is not feasible with our sample.

We would like to mention that a similar effect of a “low-dimensional” motion of pyridine was previously found in a comparative study of a  $\text{H}_1$  and a MCM-41 silica sample. In these experiments very weak, anisotropic signals were registered for the MCM-41 silica.<sup>30</sup> Our experiments show that the discussed effect has the same nature for the both  $\text{H}_1$  and MCM-41 silica and the difference has been caused, probably, because of a relatively high surface roughness of the MCM-41 sample, employed in the former study.

## Conclusions

It has been demonstrated that a combination of various solid state NMR techniques performed on mesoporous silica samples makes it possible to describe in detail the structure of mesoporous silica. Important are especially NMR experiments on pyridine and its derivatives, which can form hydrogen-bonded complexes with the surface silanol groups. By low-temperature NMR, the slow hydrogen bond exchange regime between hydrogen-bonded and non-hydrogen-bonded pyridine molecules is reached, which allows one to determine the number of pyridine molecules that are able to form hydrogen bonds to the surface OH groups. Very helpful were previous calibrations by solid-state NMR of the  $^{15}\text{N}$  chemical shifts of collidine–acid hydrogen-bonded complexes with the N...H distances and the nominal  $\text{p}K_a$  values of the acids in water. This method allows one to obtain the nitrogen–hydrogen distance distribution functions, and, using well-established hydrogen bond correlations, also the N...O distances of pyridine in porous hosts by one-dimensional  $^{15}\text{N}$  solid-state NMR at low temperatures, corroborated by  $^1\text{H}$  MAS NMR. The latter method gives an indication whether silanol groups are present in small pores or the walls of mesoporous silica, which are not exposed to hydrogen bonding with pyridine. At room temperature, the pyridine reorientation can be isotropic or anisotropic, as demonstrated by  $^{15}\text{N}$  and  $^2\text{H}$  NMR, when the chemical shifts indicate that in both cases pyridine is hydrogen bonded to the surface, the isotropic reorientation indicates that the surface is rough, i.e., that the OH bonds point in all directions of space, in contrast to the case of an anisotropic motion where certain directions are excluded. Molecular models of cylindrical pores were constructed from fused tridymite fragments, providing a variety of regular or irregular surface OH group distributions and number of silanol groups in the surfaces (Figures 9–12). From these models the hexagonal arrangement of the cylindrical pores arise in a natural way. Although these models could not be proved, they are able to accommodate almost all experimental findings. Therefore, they might serve as input for quantum-mechanical models soon. In particular, by decorating the surface of large pores with tridymite fragments as isles, equatorial and geminal silanol groups are introduced, which exhibit the OH axis in all directions of space, explaining the isotropic reorientation of pyridine during jumps from one-hydrogen bond to another, constituting the elementary steps of the pyridine surface diffusion.

**Acknowledgment.** This work was supported by the Deutsche Forschungsgemeinschaft in the framework of the Sonderforschungsbereich 448 “Mesoskopisch Strukturierte Verbundsysteme”.

### Appendix

#### Rotational Averaging of the Pyridine-<sup>15</sup>N Tensor and the <sup>2</sup>H Quadrupolar Tensor on the Inner Surfaces of the Mesopores.

In the following a model of the rotational degrees of freedom of the pyridine molecule, hydrogen bond to the inner surface of a mesopore is developed. For the following discussion it is convenient to employ different coordinate systems, namely, the molecular coordinate system of the pyridine molecule, which is the molecular  $x$  axes  $x_m, y_m, z_m$  and a pore coordinate system  $X_p, Y_p, Z_p$  with the  $z$  direction as direction of the pore, the  $x$  direction as the bond direction of the  $-\text{SiO}$  bond, and the  $y$  direction as the normal of  $X_p$  and  $Z_p$ .

Three possible rotations of the pyridine molecule are considered (see Figure 16), namely, the rotation  $R_1$  of the pyridine molecule around the direction of the hydrogen bond, which is a rotation around  $x_m$ , the rotation  $R_2$  of the  $-\text{OH}$  group around the  $-\text{SiO}$  bond direction, which is a rotation around  $X_p$ , and the rotation  $R_3$  around the pore axis  $Z_p$ , caused by the surface migration of the pyridine molecules. In the fast limit all three rotations cause an averaging of the pyridine chemical shift tensor. Assuming that the three rotations are independent of each other, we can calculate the respective averaging in a consecutive manner.

For simplicity we calculate the averages for the more general case of the CS tensor. The averages of the quadrupolar tensor are obtained by replacing the principal values of the CS tensor ( $\sigma_{xx}, \sigma_{yy}, \sigma_{zz}$ ) with the principal values of the quadrupolar tensor ( $q_{xx}, q_{yy}, q_{zz}$ ).

As a starting point we have the CS tensor of the static pyridine molecule in its principal axis system:

$$\tilde{\sigma}_0 = \begin{pmatrix} \sigma_{xx} & 0 & 0 \\ 0 & \sigma_{yy} & 0 \\ 0 & 0 & \sigma_{zz} \end{pmatrix} \quad (\text{A.1})$$

Case 1: All three rotations are possible.

For the first rotation the averaged CS tensor is given as (note:  $R_x, R_y, R_z$  are rotations around the  $x, y$ , and  $z$  axis, respectively):

$$\begin{aligned} \tilde{\sigma}_1 &= \int_0^{2\pi} R_x(\varphi) \tilde{\sigma}_0 R_x^{-1}(\varphi) d\varphi \\ &= \begin{pmatrix} \sigma_{xx} & 0 & 0 \\ 0 & \frac{1}{2}(\sigma_{yy} + \sigma_{zz}) & 0 \\ 0 & 0 & \frac{1}{2}(\sigma_{yy} + \sigma_{zz}) \end{pmatrix} \end{aligned} \quad (\text{A.2})$$

For the second rotation we first have to tilt the molecule with the angle  $\alpha$ , which is  $180^\circ$  minus the  $\text{SiOH}$  bond angle and then rotate around the  $X_p$  axis:

$$\begin{aligned} \tilde{\sigma}_2 &= \int_0^{2\pi} R_x(\psi) R_y(\alpha) \tilde{\sigma}_1 R_y^{-1}(\alpha) R_x^{-1}(\psi) d\psi \\ &= \begin{pmatrix} \cos^2 \alpha \sigma_{xx} + \frac{1}{2}(1 - \cos^2 \alpha)(\sigma_{yy} + \sigma_{zz}) & 0 & 0 \\ 0 & \frac{1}{2}(1 - \cos^2 \alpha)\sigma_{xx} + \frac{1}{4}(1 + \cos^2 \alpha)(\sigma_{yy} + \sigma_{zz}) & 0 \\ 0 & 0 & \frac{1}{2}(1 - \cos^2 \alpha)\sigma_{xx} + \frac{1}{4}(1 + \cos^2 \alpha)(\sigma_{yy} + \sigma_{zz}) \end{pmatrix} \end{aligned} \quad (\text{A.3})$$

The third rotation finally is a rotation around the pore  $Z_p$  axis:

$$\begin{aligned} \tilde{\sigma}_3 &= \int_0^{2\pi} R_z(\theta) \tilde{\sigma}_2 R_z^{-1}(\theta) d\theta \\ &= \begin{pmatrix} \frac{1}{4}(1 + \cos^2 \alpha)\sigma_{xx} + \frac{1}{8}(3 - \cos^2 \alpha)(\sigma_{yy} + \sigma_{zz}) & 0 & 0 \\ 0 & \frac{1}{4}(1 + \cos^2 \alpha)\sigma_{xx} + \frac{1}{8}(3 - \cos^2 \alpha)(\sigma_{yy} + \sigma_{zz}) & 0 \\ 0 & 0 & \frac{1}{2}(1 - \cos^2 \alpha)\sigma_{xx} + \frac{1}{4}(1 + \cos^2 \alpha)(\sigma_{yy} + \sigma_{zz}) \end{pmatrix} \end{aligned} \quad (\text{A.4})$$

Case 2: Rotations around  $\text{OH} \cdots \text{N}$  hydrogen bond is suppressed.



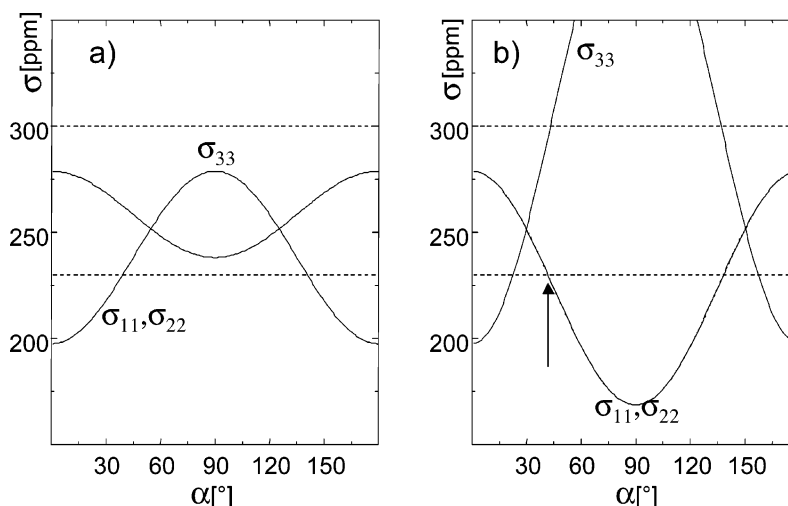


**Figure 16.** Calculated tensor eigenvalues of the two motional models: (left panel) model 1; (right panel) model 2. Note that only model 2 (arrow) is capable of fitting the experimental eigenvalues (dashed lines).

As discussed in the text from the simulation of the spectra, it is evident that the first rotation around  $\varphi$  is strongly hindered. In this case the average tensor is simply given as the result of the tilt and the rotations around  $R_x$  and  $R_z$ :

$$\tilde{\sigma}_3' = \int_0^{2\pi} R_z(\theta) \int_0^{2\pi} R_x(\psi) R_y(\alpha) \tilde{\sigma}_0 R_y^{-1}(\alpha) R_x^{-1}(\psi) d\psi R_z^{-1}(\theta) d\theta$$

$$= \begin{pmatrix} \frac{1}{4}(1 + \cos^2 \alpha)\sigma_{xx} + \frac{1}{4}\sigma_{yy} + \frac{1}{4}(2 - \cos^2 \alpha)\sigma_{zz} & 0 & 0 \\ 0 & \frac{1}{4}(1 + \cos^2 \alpha)\sigma_{xx} + \frac{1}{4}\sigma_{yy} + \frac{1}{4}(2 - \cos^2 \alpha)\sigma_{zz} & 0 \\ 0 & 0 & \frac{1}{2}(1 - \cos^2 \alpha)\sigma_{xx} + \frac{1}{2}\sigma_{yy} + \frac{1}{2}\cos^2 \alpha\sigma_{zz} \end{pmatrix} \quad (\text{A.5})$$

Figure 16 displays the dependence of the averaged eigenvalues of these tensors as a function of the angle  $\alpha$ . From the figure it is evident that in case of the first model, no angle  $\alpha$  matches the experimentally found tensor eigenvalues. In the case of the second model, however, the angle of  $46^\circ$  and the symmetry equivalent angle of  $134^\circ$  match the experimental tensor values.

## References and Notes

- (1) Beck, J. S.; Vartuli, J. C.; Roth, W. J.; Leonowicz, M. E.; Kresge, C. T.; Schmitt, K. D.; Chu, C. T. W.; Olson, D. H.; Sheppard, E. W.; McCullen, S. B.; Higgins, J. B.; Schlenker, J. L. *J. Am. Chem. Soc.* **1992**, *114*, 108340.
- (2) (a) Martin, C. R. *Science* **1994**, *266*, 1961. Tanev, P. T.; Pinnavaia, T. J. *Science* **1996**, *271*, 1267. (b) Attard, G. S.; Glyde, J. C.; Göltner, C. G. *Nature* **1995**, *378*, 366. (c) Göltner, C. G. *Angew. Chem., Int. Ed. Engl.* **1999**, *38*, 3155.
- (3) Zhao, D.; Feng, J.; Huo, Q.; Melosh, N.; Fredrickson, G. H.; Chmelka, B. F.; Stucky, G. D. *Science* **1998**, *279*, 548.
- (4) (a) Thomas, J. M. *Angew. Chem., Int. Ed.* **1999**, *38*, 3588. (b) Song, X.; Sayari, A. *Catal. Rev.-Sci. Eng.* **1996**, *38*, 329.
- (5) Ladizhansky, V.; Hodes, G.; Vega, S. *J. Phys. Chem. B* **2000**, *104*, 1939.
- (6) Gjerdaker, L.; Sorland, G. H.; Aknes, D. W. *Micropor. Mesopor. Mater.* **1999**, *32*, 305.
- (7) Aknes, D. W.; Gjerdaker, L. *J. Mol. Struct.* **1999**, *475*, 27.
- (8) Jobic, H. *Phys. Chem. Chem. Phys.* **1999**, *1*, 525.
- (9) Melnichenko, Y. B.; Schüller, J.; Richert, R.; Ewen, B.; Loong, C. K. *J. Chem. Phys.* **1995**, *103*, 2016.
- (10) Corma, A. *Chem. Rev.* **1997**, *97*, 2373.
- (11) Ciesla, U.; Schüth, F. *Micropor. Mesopor. Mater.* **1999**, *27*, 131.
- (12) Selli, E.; Forni, L. *Micropor. Mesopor. Mater.* **1999**, *31*, 129.
- (13) Sauer, J.; Ugliengo, P.; Garrone, E.; Saunders, V. R. *Chem. Rev.* **1994**, *94*, 2095.
- (14) Nawrocki, J. *J. Chromatogr. A* **1997**, *779*, 29.
- (15) Landmesser, H.; Kosslick, H.; Storek, W.; Fricke, R. *Solid State Ionics* **1997**, *101–103*, 271.
- (16) Anwander, R.; Nagl, I.; Widenmeyer, M.; Engelhardt, G.; Groeger, O.; Palm, C.; Röser, Th. *J. Phys. Chem. B* **2000**, *104*, 3532. Widenmeyer, M.; Anwander, R. *Chem. Mater.* **2002**, *14*, 1827.
- (17) Zhao, X. S.; Lu, G. O.; Whittaker, A. K.; Millar, G. J.; Zhu, H. Y. *J. Phys. Chem. B* **1997**, *101*, 6525.
- (18) Jentys, A.; Kleestorfer, K.; Vinek, H. *Micropor. Mesopor. Mater.* **1999**, *27*, 321.
- (19) Brunauer, S.; Emmett, P. H.; Teller, E. *J. Am. Chem. Soc.* **1938**, *60*, 309.
- (20) Zhuravlev, L. T. *Langmuir* **1987**, *3*, 316.
- (21) Cheng, C. F.; Zhou, W.; Park, D. H.; Klinowski, J.; Hargreaves, M.; Gladden, L. F. *J. Chem. Soc., Faraday Trans.* **1997**, *93*, 359.
- (22) Ciavalleri, B.; Ugliengo, P. *J. Phys. Chem. B* **2000**, *104*, 9491.
- (23) Gedat, E.; Schreiber, A.; Findenegg, G.; Limbach, H. H.; Buntkowsky, G. *J. Phys. Chem. B* **2002**, *106*, 1977.
- (24) Aguilar-Parrilla, R.; Claramunt, R. M.; Lopez, C.; Sanz, D.; Limbach, H. H.; Elguero, J. *J. Phys. Chem.* **1994**, *98*, 8752.
- (25) Maciel, G. E.; Haw, J. F.; Chuang, I. S.; Hawkins, B. L.; Early, T. A.; McKay, D. R.; Petrakis, L. *J. Am. Chem. Soc.* **1983**, *105*, 1230.
- (26) Ripmeester, J. A. *J. Am. Chem. Soc.* **1983**, *105*, 2925.
- (27) (a) Smirnov, S. N.; Golubev, N. S.; Denisov, G. S.; Benedict, H.; Shah-Mohammadi, P.; Limbach, H. H. *J. Am. Chem. Soc.* **1996**, *118*, 4094. (b) Smirnov, S. N.; Benedict, H.; Golubev, N. S.; Denisov, G. S.; Kreevoy, M. M.; Schowen, R. L.; Limbach, H. H. *Can. J. Chem.* **1999**, *77*, 943. (c) Golubev, N. S.; Smirnov, S. N.; Shah-Mohammadi, P.; Shenderovich, I. G.; Denisov, G. S.; Gindin, V. A.; Limbach, H. H. *Russ. J. Gen. Chem.* **1997**, *67*, 1150. (e) Shah-Mohammadi, P.; Shenderovich, I. G.; Detering, C.; Limbach, H. H.; Tolstoy, P. M.; Smirnov, S. N.; Denisov, G. S.; Golubev, N. S. *J. Am. Chem. Soc.* **2000**, *122*, 12878.
- (28) (a) Golubev, N. S.; Denisov, G. S.; Smirnov, S. N.; Shchepkin, D.; Limbach, H. H. *Z. Phys. Chem.* **1996**, *196*, 73–84. (b) Ramos, M.; Alkorta, I.; Elguero, J.; Golubev, N. S.; Denisov, G. S.; Benedict, H.; Limbach, H. H. *J. Phys. Chem.* **1997**, *A101*, 9791–9800. (d) Golubev, N. S.; Shenderovich, I. G.; Smirnov, S. N.; Denisov, G. S.; Limbach, H. H. *Chem. Eur. J.* **1999**, *5*, 492. (c) Shenderovich, I. G.; Burtsev, A. P.; Denisov, G. S.; Golubev, N. S.; Limbach, H. H. *Magn. Reson. Chem.* **2001**, *39*, S91.
- (29) Lorente, P.; Shenderovich, I. G.; Benedict, H.; Golubev, N. S.; Limbach, H. H. *Magn. Reson. Chem.* **2001**, *39*, S18.
- (30) Edgar, M.; Schubert, M.; Limbach, H. H.; Göltner, C. G. *Ber. Bunsen-Ges. Phys. Chem.* **1997**, *101*, 1769.

- (31) Gedat, E.; Schreiber, A.; Findenegg, G.; Limbach, H. H.; Buntkowsky, G. *Magn. Reson. Chem.* **2001**, *S39*, 148.
- (32) Grün, M.; Unger, K. K.; Matsumoto, A.; Tsutsumi, K. *COPS IV* **1997**, 81–89.
- (33) (a) Schreiber, A.; Ketelsen, I.; Findenegg, G. H. *Phys. Chem. Chem. Phys.* **2001**, *3*, 1185. (b) Schreiber, A. Ph.D. Thesis, Technische Universität Berlin, 2002.
- (34) Hildebrand, U.; Taraz, K.; Budzikiewicz, H. *J. Labelled Compd. Radiopharm.* **1984**, *22*, 293.
- (35) Hunger, M. Technical University of Stuttgart, personal communication.
- (36) Engelhardt, G.; Koller, H. *NMR Basic Principles Prog.* **1994**, *31*, 1.
- (37) Buntkowsky, G.; Sack, I.; Limbach, H. H.; Kling, B.; Fuhrhop, J. *J. Phys. Chem. B* **1997**, *101*, 11265.
- (38) Wehrmann, F.; Fong, T.; Morris, R. H.; Limbach, H. H.; Buntkowsky, G. *Phys. Chem. Chem. Phys.* **1999**, *1*, 4033.
- (39) Mehring, M. *High-Resolution NMR Spectroscopy in Solids*; Springer-Verlag: Berlin, Heidelberg, New York, 1983.
- (40) Kolodziejewski, W.; Corma, A.; Navarro, M. T.; Perez-Pariente, J. *Solid State Nucl. Magn. Reson.* **1993**, *2*, 253.
- (41) Fu, G. U.; Fyfe, C. A.; Schwieger, W.; Kokotailo, G. T. *Angew. Chem., Int.* **1995**, *34*, 1499.
- (42) (a) Solum, M. S.; Altmann, K. L.; Strohmeier, M.; Berges, D. A.; Zhang, Y.; Facelli, J. C.; Pugmire, R. J.; Grant, D. M. *J. Am. Chem. Soc.* **1997**, *119*, 9804. (b) Schweitzer, D.; Spiess, H. W. *J. Magn. Reson.* **1974**, *15*, 529.
- (43) Steiner, Th. *J. Phys. Chem. A* **1998**, *102*, 7041–7052.
- (44) Haase, F.; Sauer, J. *Micropor. Mesopor. Mater.* **2000**, *35–36*, 379.
- (45) *CRC Handbook of Chemistry and Physics*; Lide, D. R., Ed.; CRC Press LLC: London, New York, 2000–2001; p 81.
- (46) Kagiya, T.; Sumida, Y.; Tachi, T. *Bull. Chem. Soc. Jpn.* **1970**, *43*, 3716.
- (47) Marshall, K.; Ridgewell, G. L.; Rochester, C. H.; Simpson, J. *J. Chem Ind. (London)* **1974**, 775.
- (48) De Boer, J. H.; Vleeskens, J. M. *Proc. K. Ned. Akad. Wet., Ser. B Phys. Sci.* **1958**, *61*, 2. De Boer, J. H. *Angew. Chem.* **1958**, *70*, 383.
- (49) Kihara, K. *Z. Kristallographie* **1980**, *152*, 95; **1981**, *157*, 93. CIF file 30795-ICSD from the Inorganic Cambridge Structure Database (ICSD).
- (50) We found in the Inorganic Cambridge Structure Database (ICSD) 238 silicon dioxide crystal structures comprising different variations of the following crystal types: quartz (79); stishovite (28); cristobalite (26); coesite (16); tridymite (13); others (29); and several zeolite (47) structures (ZSM-11; ZSM-12; ZSM-22; CIT-5; ITQ-1; ITQ-3; ITQ-7; RUB-3; SSZ-31; UTD-1; and others).
- (51) Spohr, E.; Hartnig, C.; Gallo, P.; Rovere, M. *J. Mol. Liq.* **1999**, *80*, 165.
- (52) Spohr, E. Personal communication.